1

Improved Prediction of Dimethyl Sulfide (DMS) Distributions in the NE Subarctic Pacific using Machine Learning Algorithms

Brandon J. McNabb[1] & Philippe D. Tortell[1,2]

[1]Department of Earth, Ocean and Atmospheric Sciences, University of British Columbia, Vancouver, BC V6T 1Z4, Canada

[2]Department of Botany, University of British Columbia, Vancouver, BC V6T 1Z4, Canada

Correspondence to: Brandon J. McNabb (bmcnabb@eoas.ubc.ca)

Abstract. Dimethyl sulfide (DMS) is a volatile biogenic gas with the potential to influence regional climate as a source of atmospheric aerosols and cloud condensation nuclei (CCN). The complexity of the oceanic DMS cycle presents a challenge in accurately predicting sea-surface concentrations and sea-air fluxes of this gas. In this study, we applied machine learning methods to model the distribution of DMS in the NE Subarctic Pacific (NESAP), a global DMS hot-spot. Using nearly two decades of ship-based DMS observations, combined with satellite-derived oceanographic data, we constructed ensembles of 1000 machine-learning models using two techniques, random forest regression (RFR) and artificial neural networks (ANN). Our models dramatically improve upon existing statistical DMS models, capturing up to 62% of observed DMS variability in the NESAP and demonstrating notable regional patterns that are associated with mesoscale oceanographic variability. In particular, our results indicate a strong coherence between DMS concentrations, sea surface nitrate (SSN) concentrations, photosynthetically active radiation (PAR) and sea surface height anomalies (SSHA), suggesting that NESAP DMS cycling is primarily influenced by heterogenous nutrient availability, light-dependent processes and physical mixing. Based on our model output, we derive summertime, sea-air flux estimates of 1.16±1.22 Tg S in the NESAP. Our work demonstrates a new approach to capturing spatial and temporal patterns in DMS variability, which is likely applicable to other oceanic regions.

1 Introduction

Dimethyl sulfide (DMS), a volatile biogenic gas, is an important component of the marine sulfur cycle. This molecule is an important substrate for specific methylotrophic bacteria (Vila-Costa et al., 2006; Lidbury et al., 2016; Green et al., 2011; Hatton et al., 2012), with a recognized importance to marine microbial metabolism (Vila-Costa et al., 2006) and food web interactions (Nevitt, 2008). Moreover, DMS constitutes the largest fraction of bulk non-sea salt (NSS) sulfate emissions to the atmosphere (Bates et al., 1992; Ksionzek et al., 2016), where it is rapidly oxidized to form aerosols that act as cloud condensation nuclei (CCN; Charlson et al., 1987; Hegg et al., 1991; Korhonen et al., 2008), potentially influencing regional albedo and climate (Charlson et al., 1987; Ayers and Cainey, 2007). Given the ecological roles of DMS and its potential influence on global climate, substantial research has focused on characterizing the dynamics of this compound in seawater. This work has revealed considerable complexity in the oceanic DMS cycle, which has limited the development of simple predictive algorithms describing its spatial and temporal variability.

Oceanic DMS production and loss are tightly linked with the biological cycling of the related metabolites dimethyl sulfoniopropionate (DMSP) and dimethyl sulfoxide (DMSO). DMS is believed to be primarily derived

from the cleavage of DMSP (Kiene and Linn, 2000), but it can also be cycled through biological DMSO reduction (Spiese et al., 2009) and oxidation (Lidbury et al., 2016), and abiotically by light-dependent reactions (del Valle et al., 2007; Royer et al., 2016). DMS cycling is influenced by a suite of environmental and ecological factors, including release from phytoplankton cells into the dissolved pool via grazing (Dacey and Wakeham, 1986), viral lysis (Malin et al., 1998), or exudation. Oxidative stress generated by other variables such as temperature (Kirst et al., 1991), salinity (Dickson and Kirst, 1987), UV radiation (Kinsey et al., 2016), and nutrient limitation (Bucciarelli et al., 2013; Spiese & Tatarkov, 2014) may also enhance the cycling of DMSP and DMSO, which may regulate DMS concentrations through cascading oxidative pathways (Sunda et al., 2002). Finally, variability in surface wind fields can modulate the rates of DMS sea-air exchange, providing a significant source of heterogeneity in surface water DMS concentrations (Royer et al., 2016). These examples illustrate the complex non-linearity of the oceanic DMS cycle.

Over the past two decades, a number of approaches have been developed to model DMS distributions at both global (Bock et al., 2021; Galí et al., 2018; Simó and Dachs, 2002; Vallina and Simó, 2007) and regional (Watanabe et al., 2007) scales. These models have been largely based on linear regression techniques estimating DMS concentrations using one or two predictors. To date, these studies have focused on a number of variables, including ratio of chlorophyll a (Chl-a) to mixed layer depth (MLD) (Simó and Dachs, 2002), sea surface temperature (SST) and nitrate (SSN) (Watanabe et al., 2007), solar radiation dose (SRD) (Vallina and Simó, 2007), photosynthetically active radiation (PAR) and modelled DMSP concentrations (Galí et al., 2018). Some of these models have demonstrated reasonably good performance at global scales, but their predictive power is generally diminished at regional scales (Herr et al., 2019), failing to accurately resolve important smaller-scale features (Belviso et al., 2003; Nemcek et al., 2008; Royer et al., 2015; Tortell, 2005b).

In recent years, machine-learning algorithms have been increasingly used to derive predictions for non-linear oceanic systems. For example, these methods have been successfully applied to describe the spatial and temporal patterns of global methane flux (Weber et al., 2019), nitrous oxide dynamics (Yang et al., 2020), and carbon export (Roshan and DeVries, 2017). To our knowledge, only two studies have thus far applied machine-learning to describe DMS distributions, with one study focused on the Arctic (Humphries et al., 2012) and the other exploring a global domain (Wang et al., 2020). Despite producing algorithms with reasonable predictive skill, these two studies found limited success in resolving the underlying relationships driving DMS variability. This was partially due to a reliance on indirect sensitivity tests assessing the importance of predictor variables, and also, potentially, from the large-scale averaging applied to the underlying data fields (1x1°; 111 km^2). Analyses at higher

68 spatial resolution may reveal mesoscale (roughly 20-200 km) and sub-mesoscale (roughly 1-20 km) patterns that

69 would otherwise be obscured, thereby increasing predictive strength.

70   Machine learning algorithms require large datasets for the training and testing process. Traditionally, DMS

71 measurements were based on time-consuming ship-board analysis of discrete samples, resulting in sparse data

72 coverage over much of the oceans. More recently, the development of several automated DMS measurement

73 systems (Royer et al., 2014; Saltzman et al., 2009; Tortell, 2005a) has provided marine DMS observations at a

74 significantly higher resolution, yielding greater spatial and temporal data coverage. These new datasets potentially

75 enable new insights into small-scale and regional patterns in oceanic DMS distributions, as well as the

76 characterization of oceanic DMS 'hot-spots'. The northeast subarctic Pacific (NESAP) is a region of notably high

77 DMS concentrations (Lana et al., 2011), with localized DMS accumulation in both highly productive coastal

78 upwelling regimes, and off-shore, iron-limited waters (Herr et al., 2019; Asher et al., 2017). Several factors have

79 been proposed to account for the elevated DMS production in the NESAP, including increased primary productivity

80 driven by nutrient entrainment and upwelling along coastal fronts (Asher et al., 2017), a dominance of high-DMSP

81 producing prymnesiophytes and dinoflagellates in offshore waters, elevated microbial degradation of DMSP to

82 DMS (Steiner et al., 2012; Royer et al., 2010), and the stimulation of DMS production in response to oxidative

83 stress in low iron waters (Sunda et al., 2002; Herr et al., 2020). Although multiple studies have examined empirical

84 relationships between DMS and various oceanographic factors in the NESAP (Watanabe et al., 2007; Herr et al.,

85 2019; Asher et al., 2017, 2011), these have all reported low predictive skill based on simple linear correlation

86 approaches. To date, machine-learning approaches have not been applied to describe DMS distributions specifically

87 in this region.

88   Here, we present an approach to modelling summertime NESAP DMS concentrations and sea-air fluxes

89 using ensemble random forest regression (RFR) and artificial neural network (ANN) machine-learning algorithms.

90 Our statistical models leverage field observations of DMS collected across the NESAP between 1997 to 2017 to

91 generate a summertime DMS climatology mapped at a higher spatial resolution than previous efforts (Simó and

92 Dachs, 2002; Vallina and Simó, 2007; Galí et al., 2018; Watanabe et al., 2007; Humphries et al., 2012; Wang et

93 al., 2020). This new modelling approach represents a significant improvement over previous methods and predicts

94 regional DMS distributions that are coherent with underlying patterns of oceanographic variability. Most notably,

95 the modelled DMS concentrations and sea-air fluxes can be explained, to a large extent, by regional and mesoscale

96 patterns in nutrient supply and physical mixing dynamics. Based on the output of our models, we present

97 summertime sea-air flux estimates in close agreement with previous studies (Herr et al., 2019; Lana et al., 2011),

98 further highlighting the importance of the NESAP as a globally-significant sulfur source to the atmosphere.

2 Methods

2.1 Data

A combination of data sources was used in training our machine-learning models to build a summertime DMS climatology. For this study, we restricted DMS measurements to the months of June, July and August between 1997 to 2017 in the NESAP (43-60°N, 147-122°W). A total of 26,201 data points were obtained from the NOAA PMEL repository (https://saga.pmel.noaa.gov/dms/; last accessed: February 3, 2021), including measurements derived from purge and trap gas chromatography and membrane inlet mass spectrometry. The DMS data were binned to a monthly resolution, regardless of year, and averaged into 0.25 x 0.25° grid cells.

Predictor data used to build our machine-learning models included the following variables derived from the NASA Aqua MODIS satellite at level L3 monthly 0.042° resolution (R2018.0): sea surface temperature (SST), the ratio of normalized fluorescence line height to chlorophyll a (nFLH:Chl-a), instantaneous and daily observed photosynthetically active radiation (iPAR and PAR, respectively), particulate inorganic carbon (PIC), the absorption of gelbstof and detritus at 433 nm ($a_{cdm}(443)$), and diffuse attenuation coefficients at 490nm (K_d). Satellite-based PIC is considered as a proxy for the abundance of coccolithophores and other calcified phytoplankton (Franklin et al., 2010), whereas the $a_{cdm}(443)$ product is considered a proxy for chromophoric dissolved organic matter (CDOM; Nelson & Siegel, 2013), which is thought to be an important photosensitizer of DMS (see Sect. 4.1). For observations prior to 2004, data were from either SeaWiFS (0.083° resolution) or Terra MODIS (0.042° resolution) when SeaWiFS data were unavailable (*e.g.* nFLH and iPAR). As described below, K_d and PIC were later excluded from the final models (see Sect. 2.6), as they didn't improve predictive skill.

The following predictor variables were also used: 6-day averaged sea surface height anomalies (SSHA) derived from the TOPEX/Poseidon satellites at 0.17° resolution; Level L4 ESA Sentinal-3 Copernicus monthly-averaged 0.25° wind speeds; net primary productivity (NPP) from the Vertically-Generalized Production Model (VGPM; Behrenfeld & Falkowski, 1997) at monthly 0.25° resolution; sea surface nitrate from the 2018 World Ocean Atlas at monthly 1° resolution (Garcia et al., 2019); and mixed-layer depth (MLD) and sea surface salinity (SSS) from the MIMOC climatology at 0.5° resolution (Schmidtko et al., 2013). Except for MIMOC data, all predictors were restricted in time to the corresponding years of DMS sampling (1997 to 2017). Net community productivity (NCP) was estimated from the algorithm of Li & Cassar, (2016; using NPP and SST). As with DMS observations, predictor data were interpolated to a 0.25 x 0.25° average monthly resolution using linear radial basis interpolation functions. Interpolation was constrained to the oceanic region by masking out land pixels using ETOPO2 bathymetric (0.033° resolution) binned at 0.25 x 0.25° resolution. We note that each of these data sources

129 are likely to have inherent uncertainties associated with either their collection or processing. Data sources can be

130 found in Table 1.

131

132 **Table 1. Data sources and spatial and temporal resolution of predictor variables used to develop the RFR and ANN algorithms. Data**
133 **processing levels are indicated where relevant. All variables were used as predictors (excluding bathymetry) and post-processed to**
134 **monthly-averaged, 0.25º resolution (see sections 2.1-2.2).**

Variable	Spatial Resolution (º)	Temporal Resolution	Source	Level
Sea Surface Temperature (SST)	0.042	6-Day Average	SeaWiFS/AquaTERRA (1997-2003) or AquaMODIS(2004-2017): https://oceancolor.gsfc.nasa.gov/l3/	3
Chlorophyll-Normalized Fluorescence (nFLH:Chl-a)	0.042	Monthly	SeaWiFS/AquaTERRA (1997-2003) or AquaMODIS (2004-2017): https://oceancolor.gsfc.nasa.gov/l3/	3
Instantaneous Photosynthetically Active Radiation (iPAR)	0.042	Monthly	SeaWiFS/AquaTERRA (1997-2003) or AquaMODIS (2004-2017): https://oceancolor.gsfc.nasa.gov/l3/	3
Daily Photosynthetically Active Radiation (PAR)	0.042	Monthly	SeaWiFS/AquaTERRA (1997-2003) or AquaMODIS (2004-2017): https://oceancolor.gsfc.nasa.gov/l3/	3
Particulate Inorganic Carbon (Calcite; PIC)	0.042	Monthly	SeaWiFS/AquaTERRA (1997-2003) or AquaMODIS (2004-2017): https://oceancolor.gsfc.nasa.gov/l3/	3
Absorption of Gelbstof and Detritus at 433 nm ($a_{cdm}(443)$)	0.042	Monthly	SeaWiFS/AquaTERRA (1997-2003) or AquaMODIS (2004-2017): https://oceancolor.gsfc.nasa.gov/l3/	3
Diffuse Attenuation Coefficients at 490 nm (K_d)	0.042	Monthly	SeaWiFS/AquaTERRA (1997-2003) or AquaMODIS (2004-2017): https://oceancolor.gsfc.nasa.gov/l3/	3
Sea Surface Height Anomalies (SSHA)	0.17	Monthly	TOPEX/Poseidon: https://podaac.jpl.nasa.gov/dataset/SEA_SURFACE_HEIGHT_ALT_GRIDS_L4_2SATS_5DAY_6THDEG_V_JPL1812	4
Monthly Wind Speeds	0.25	Monthly	ESA Sentinal-3 Copernicus: https://resources.marine.copernicus.eu/?option=com_csw&view=details&product_id=WIND_GLO_PHY_CLIMATE_L4_REP_012_003	N/A

Net Primary Productivity (NPP)	0.25	Monthly	Vertically-Generalized Production Model (VGPM): http://www.science.oregonstate.edu/ocean.productivity/	N/A
Sea Surface Nitrate (SSN)	1	Monthly	World Ocean Atlas 2018 (WO18): https://www.ncei.noaa.gov/access/world-ocean-atlas-2018/	N/A
Mixed Layer Depth (MLD)	0.5	Monthly	MIMOC Climatology: https://www.pmel.noaa.gov/mimoc/	N/A
Sea Surface Salinity (SSS)	0.5	Monthly	MIMOC Climatology: https://www.pmel.noaa.gov/mimoc/	N/A
Bathymetry	0.033	N/A	ETOPO2: https://rda.ucar.edu/datasets/ds759.3/	N/A

135

2.2 Machine-learning models

We compared the performance of random forest regression (RFR) and artificial neural network (ANN) models at the regional scale. The RFR algorithm is built upon decision tree models, which operate by iteratively generating decision rule nodes that dictate which branch the tree will progress through in the next iteration. The RFR model builds an ensemble, or "forest", of these trees, where each tree is trained on a bootstrapped (*i.e.* randomly subsampled) set of predictors, and the resulting predictions are averaged among the trees to reduce overfitting to noise (Brieman, 2001). In contrast, the ANN model is built as a fully connected network of nodes, or "neurons", in which each neuron consists of an activation function and is connected to other neurons by iteratively-determined weights (Gardner and Dorling, 1998). Both algorithms are advantageous because they make no prior assumptions on the data distributions and can fit non-linear data (Brieman, 2001; Gardner and Dorling, 1998).

Both our ANN and RFR models followed a similar design to Weber et al. (2019). Our ANNs were built using a feed-forward framework consisting of a single input node, two hidden layers each consisting of 30 neurons (using a sigmoidal activation function), and a single output layer (using a linear activation function). A Bayesian L2 (Ridge) regularization parameter was tuned to minimize overfitting and the L-BFGS algorithm was used to solve for weights (Byrd et al., 1995). Each individual decision tree within the RFR was trained using the standard CART algorithm (Brieman, 2001) and constrained to a max depth of 25 decision splits, the simplest configuration determined to perform well and minimize overfitting. These models were built using the Scikit-Learn (v0.24.2) implementation of the ANN ("MLPRegressor") and RFR ("RandomForestRegressor") algorithms in Python 3.8 (see Code Availability).

In both cases, the models were built as an ensemble of either 1000 individual decision trees or individual networks to minimize bias in predictions. The input data were randomly divided for use in model training (80%) and external testing (20%). Although RFR is not sensitive to large differences in predictor variance, predictor data were standardized in both models by normalization to their respective mean and standard deviation. Additionally, we applied an inverse hyperbolic sine (IHS) transformation to the DMS data prior to training (Weber et al., 2019). Testing results indicated that IHS yielded slightly better performance than the more traditional logarithmic transformations for both of our models.

2.3 Sea-to-air fluxes

Sea-air DMS fluxes (F_{DMS}, µmol m^{-2} d^{-1}) were calculated from the monthly-averaged observed and modelled DMS values for June, July and August. F_{DMS} was calculated using the gas transfer velocity (k, cm hr^{-1}) following the modified approach of Webb et al. (2019):

$$F_{DMS} = k(DMS)(0.24) \tag{1}$$

where the factor of 0.24 converts to the values to daily fluxes. The gas transfer velocity has typically been calculated using a non-linear parameterization (Nightingale et al., 2000), but recent work has suggested a linear parameterization is more appropriate for DMS (Bell et al., 2013; Blomquist et al., 2017; Zavarsky et al., 2018). Since satellite-derived predictors are used to build our models, we calculated the gas transfer velocity using the linear Goddijn-Murphy et al. (2012) k parameterization, which is both derived from satellite altimeter data and normalized to a Schmidt number of 660:

$$k_{w,660} = 2.1U_{10} - 2.8 \tag{2}$$

Where U_{10} is the wind speed (m s^{-1}) at 10 m above sea surface.

Regional summertime fluxes ($\bar{F}_{DMS}$, Tg) were calculated as the average (±SD) quantity of DMS-sulfur emitted over 92 days (June, July and August) through the area of the mapped study region (1.28×10^7 km^2 or 85.0% of the total bounded area).

2.4 Comparison against existing algorithms

Simple linear regression (LR) and multiple linear regression (MLR) models were built for comparison against the machine-learning algorithms. We also tested the performance of our RFR and ANN models against the published algorithms of Simó & Dachs (2002), Watanabe et al. (2007), Vallina & Simó, (2007), and Galí et al. (2018) (hereafter referred to as SD02, W07, VS07, and G18, respectively). Solar radiation dose, SRD, used in the VS07 algorithm was calculated using MLD as described by Vallina & Simó (2007):

$$SRD = \frac{PAR}{K_d \times MLD} \times (1 - e^{-K_d \times MLD}) \tag{4}$$

Each of the four algorithms was assessed using both their original coefficients and coefficients tuned to our NESAP dataset using nonlinear least-squares optimization at both 0.25° and 1° spatial resolution (Table 2). In each case, the algorithms were run using the same monthly-averaged predictors used to develop the RFR and ANN ensembles (see Sec. 2.1). Predictors were spatially matched to either the full DMS dataset (*i.e.* all monthly averaged DMS observations) or to only the Testing partitioned dataset (see Sec. 2.2) for direct comparison with the RFR and ANN ensemble performance (Fig. 2, Table 2).

2.5 Controls on DMS variability

Principal component analysis (PCA) was applied to assess the relationships between DMS and the nine predictors used to build the RFR and ANN ensembles. Additionally, non-parametric Spearman rank correlations were calculated between each variable and both the modelled and observed DMS concentrations. Correlation analysis was also extended to assess the role of taxonomy on predicted DMS concentrations, using the outputs of a chlorophyll-a based taxonomic algorithm by Hirata et al. (2011) with NESAP-tuned coefficients (Zeng et al., 2018).

2.6 Sensitivity Tests and Predictor Selection

To inform our selection of grid size, we assessed the performance of both the RFR and ANN models using grid cells ranging from 0.25 to 5° (Fig. 1). From this analysis, we found that model accuracy was highest at 0.25° resolution (see Sect. 3.1). Smaller grid sizes would presumably further improve model accuracy, but at a significantly higher computational cost.

We also tested the influence of other biological predictor variables on the performance of the RFR and ANN models, using either NCP, NPP, Chl-a, or PIC. These sensitivity tests indicated no significant difference between the various biological predictor variables, although accuracy was slightly reduced when PIC was used. We therefore selected NCP as the biological predictor variable within our model framework. We also removed K_d as a predictor variable after further sensitivity testing indicated that its exclusion slightly improved results.

The inclusion of nFLH:Chl-a represents a proxy for iron limitation (see Sect. 4.1). However, fluorescence yields corrected for non-photochemical quenching (NPQ) have been suggested to yield a better iron limitation proxy than nFLH:Chl-a (Behrenfeld et al., 2009). We therefore calculated NPQ-corrected fluorescence yields (φ_f) by:

$$\varphi_f = \frac{nFLH}{Chl-a \times \alpha \times S} \times \frac{iPAR}{\overline{iPAR}} \tag{5}$$

where $\alpha = 0.0147 \times Chl-a^{-0.316}$ and S = 100 mW cm^{-2} µm^{-1} sr^1 m as described by Behrenfeld et al. (2009). Our tests indicated nFLH:Chl-a yielded slightly improved performance overall, whereas φ_f decreased both models' performance. We therefore retained nFLH:Chl-a and excluded φ_f in our final model design.
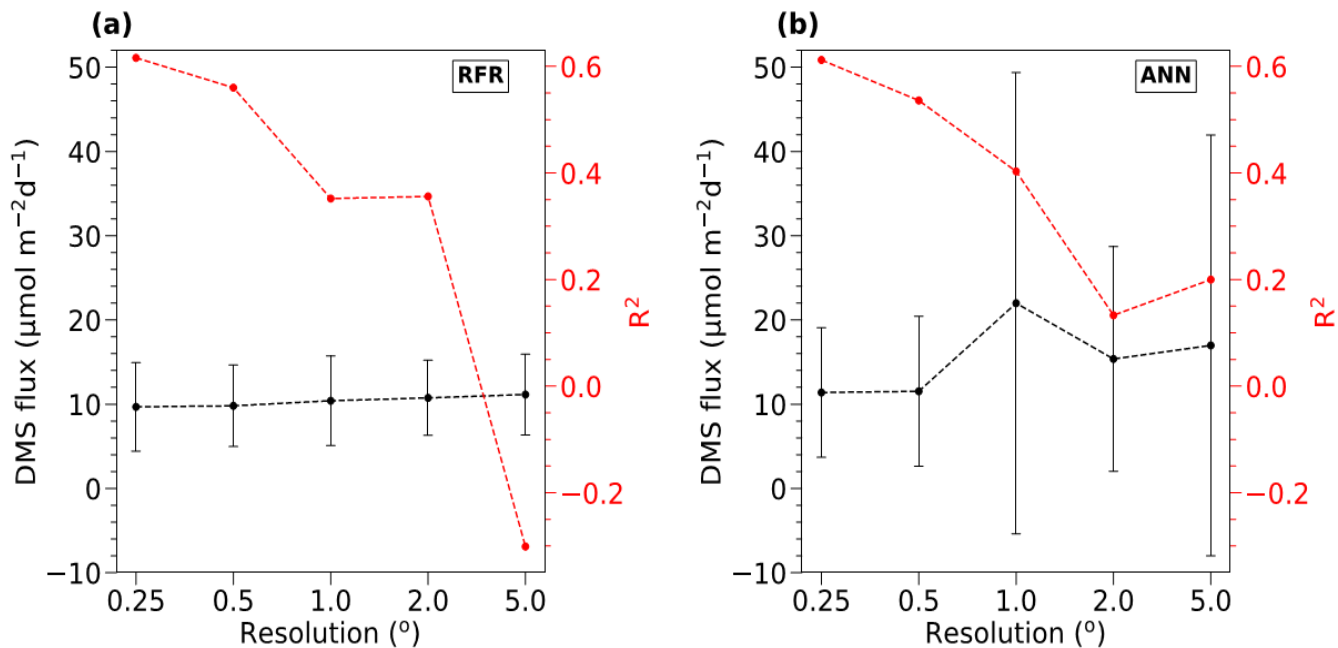
Fig. 1. Sensitivity of RFR and ANN models to grid size resolution. DMS fluxes (black) and R^2 values (red) derived from sensitivity tests of (a) RFR and (b) ANN models to pixels resolutions of 0.25-5°. The negative R^2 values observed at the lowest resolution (largest grid cells) indicate that the predicted values explain less variance than the overall mean of the dataset.

3 Results

3.1 Model evaluation

To benchmark the performance of our RFR and ANN models, we first evaluated the predictive skill of four existing empirical DMS algorithms (SD02, W07, VS07, & G18), in addition to simple and multiple linear regression models. Previous studies have demonstrated that these empirical algorithms show strong predictive skill (R^2=0.53-0.84) over large scales and in some oceanic regions (Simó and Dachs, 2002; Galí et al., 2018; Watanabe et al., 2007), but significantly poorer performance in the NESAP (Herr et al., 2019). Consistent with these results, we found that the SD02, W07, VS07, and G18 did not accurately predict NESAP DMS distributions, even with regionally tuned coefficients improving performance (Fig. 2, R^2=0-0.01 at 0.25x0.25°; Table 2, r=-0.15-0.36). We also found that simple and multiple linear regressions performed poorly, yielding virtually no explanatory power for surface water DMS distributions in the NESAP (R^2=0-0.05; Fig. 2, 3).

Table 2. Performance of statistical DMS algorithms on NESAP DMS observations binned to monthly 1° and 0.25° resolution. Pearson correlation coefficients (r) and root mean square error (nM) are obtained from the

SD02, VS07, W07 and G18 algorithms (see 2.4) using either their original published coefficients or coefficients derived from non-linear least squares optimization. Algorithm performance is evaluated using either the full monthly-binned observational dataset or using the Testing partitioned dataset (see Sec. 2.2).

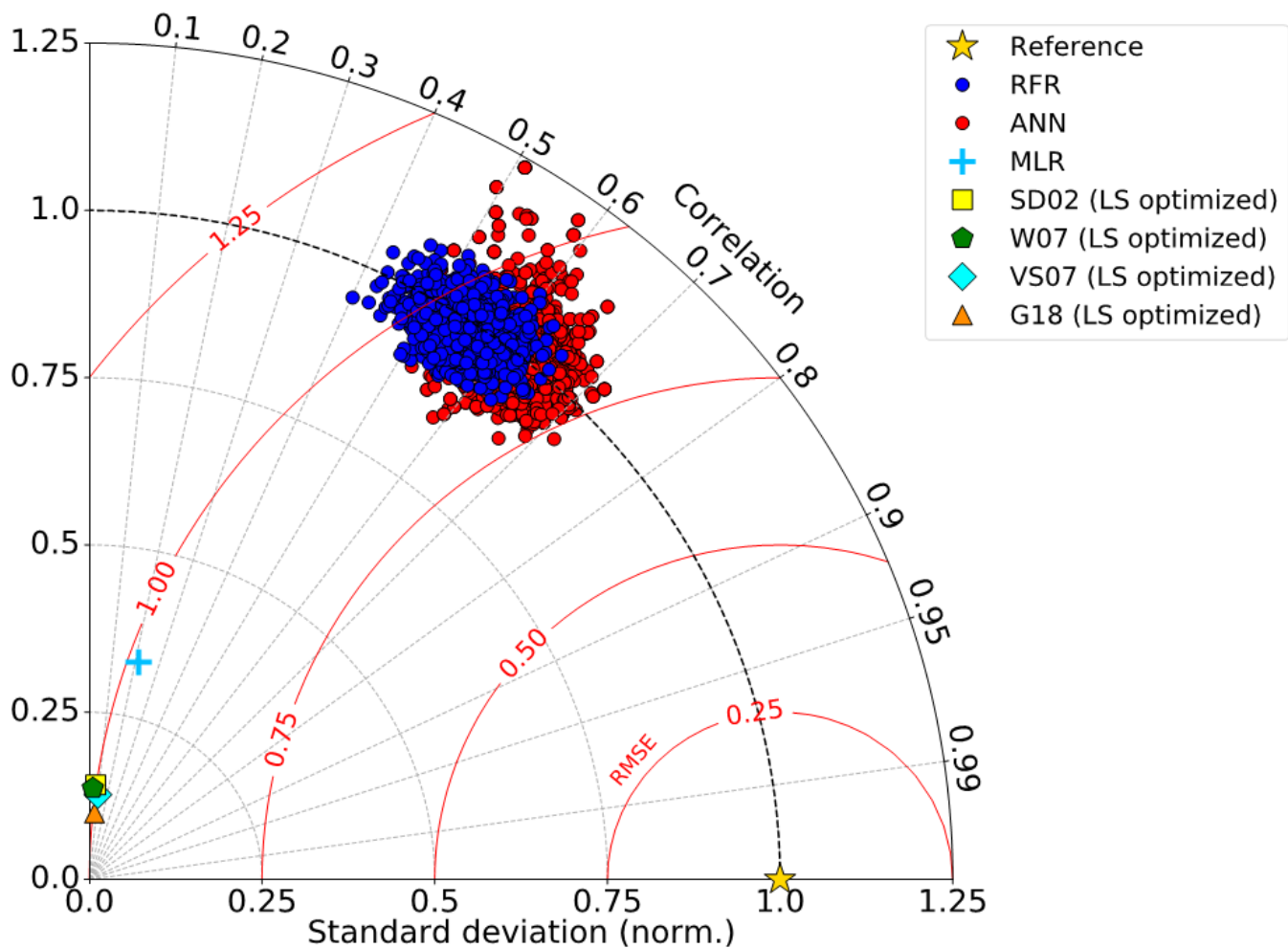|	SD02		VS07		W07		G18	
	Original	Optimized	Original	Optimized	Original	Optimized	Original	Optimized
1º All data	r = -0.09 RMSE = 18.03	r = 0.17 RMSE = 4.82	r = -0.03 RMSE = 6.67	r = 0.03 RMSE = 4.96	r = -0.10 RMSE = 11.74	r = 0.07 RMSE = 4.83	r = 0.02 RMSE = 6.77	r = 0.16 RMSE = 4.84
1º Testing dataset	r = -0.22 RMSE = 19.09	r = 0.36 RMSE = 3.34	r = 0.11 RMSE = 5.36	r = 0.20 RMSE = 3.47	r = -0.03 RMSE = 10.46	r = 0.02 RMSE = 3.47	r = -0.15 RMSE = 6.19	r = 0.30 RMSE = 3.40
0.25º All data	r = -0.05 RMSE = 11.02	r = 0.12 RMSE = 7.84	r = -0.09 RMSE = 9.57	r = 0.11 RMSE = 7.88	r = -0.09 RMSE = 13.02	r = 0.04 RMSE = 7.80	r = 0.06 RMSE = 8.42	r = 0.09 RMSE = 7.88
0.25º Testing dataset	r = -0.03 RMSE = 9.79	r = 0.07 RMSE = 6.79	r = -0.09 RMSE = 8.60	r = 0.10 RMSE = 6.79	r = -0.06 RMSE = 12.02	r = 0.04 RMSE = 6.78	r = 0.04 RMSE = 7.47	r = 0.08 RMSE = 6.80

Fig. 2. Taylor Diagram showing comparative performance metrics of each individual Random Forest Regression (RFR) and Artificial Neural Network (ANN) model (1000-model ensembles) against multiple linear regression (MLR) and other statistical DMS models (See sections 2.1 and 2.4). The Pearson correlation coefficients ("Correlation"; outer radius), root mean squared error ("RMSE"; red radial contours), and standard deviations (SDs; grey radial contours from origin) are all computed with respect to the observed DMS samples after inverse hyperbolic sine (IHS) transformation. The reference of a perfect model fit is shown with a gold star. SDs of the model outputs are normalized to the SDs of the DMS observations. RMSE represents a normalized trigonometric derivation from both the correlation coefficients and normalized SDs. Performance of the SDO2, W07, VS07, and G18 algorithms reported here are calculated using regionally tuned coefficients to the NESAP derived from non-linear least-squares optimization (see section 2.4).

Relative to other published modelling approaches, both the RFR and ANN models dramatically improved the representation of NESAP DMS variability, achieving significantly higher predictive accuracy (Fig. 2, 3). The collective ensembles of both the RFR and ANN models yielded strong performance, explaining up to 62% of the observed DMS variability (R^2=0.61-0.62; Fig. 3). For individual models within the ensembles, the ANN method

13

256 provided slightly better results (R^2=0.16-0.50), compared to the individual RFR models (R^2=0.16-0.43). However,
257 predicted DMS concentrations and sea-air fluxes derived from the ANN ensembles were more sensitive to the
258 spatial resolution used, although the predictive accuracy of both models degraded significantly with coarser
259 resolutions (Fig. 1).

260

261
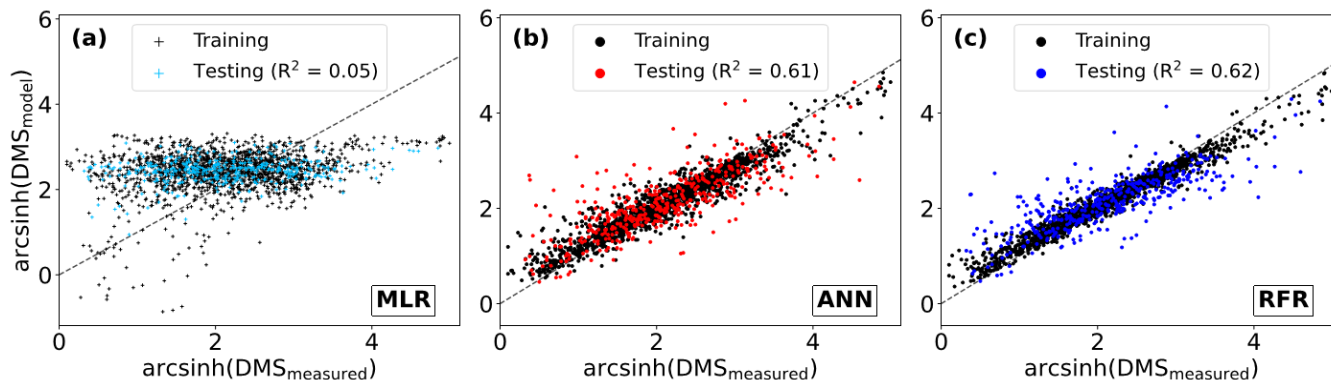
262 **Fig. 3. Performance of three modelling approaches in predicting observed DMS distributions; (A) multiple linear**
263 **regression (MLR) (B) ensemble of Artificial Neural Networks (ANN) and (C) ensemble of Random Forest Regression**
264 **(RFR). For consistency, all predictions are partitioned by the Training and Testing datasets used to build the ensembles**
265 **(see section 2.2). Model performance (R^2) is computed only for the Testing dataset predictions. The dashed line**
266 **demonstrates a 1:1 relationship. Modelled DMS concentrations depicted range from 0.4-84.3 (RFR, nM) and 0.3-74.6**
267 **(ANN, nM).**

268 **3.2 DMS distributions and sea-air fluxes**

269   In both the RFR and ANN methods, the predicted spatial distribution of DMS was generally consistent with
270 observations (Fig. 4a,c,d). The average model derived DMS concentrations was 4.0 ± 2.1 nM and 4.7 ± 3.0 nM
271 (mean $\pm$ SD) for the RFR and ANN ensemble models, respectively, with a similar range from 0.3 to 84.3 nM. In
272 both models, the highest DMS concentrations were largely constrained to coastlines and within the Alaska Gyre
273 adjacent to the Aleutian Islands (Fig. 4b-c, 8C). The greatest discrepancy between DMS concentrations from the
274 two models was observed in these regional 'hotspots', where the ANN models emphasize high DMS within the
275 Alaska gyre, while the RFR models emphasize elevated coastal DMS concentrations (Fig. 4b). On average, the
276 models deviated from each other by 0.49 nM, with the greatest offsets observed in an area of particularly sparse
277 DMS observations in the Alaska Gyre (Fig. 4a,b). Future observational data in this region should help improve
278 model agreement.

279

280

14
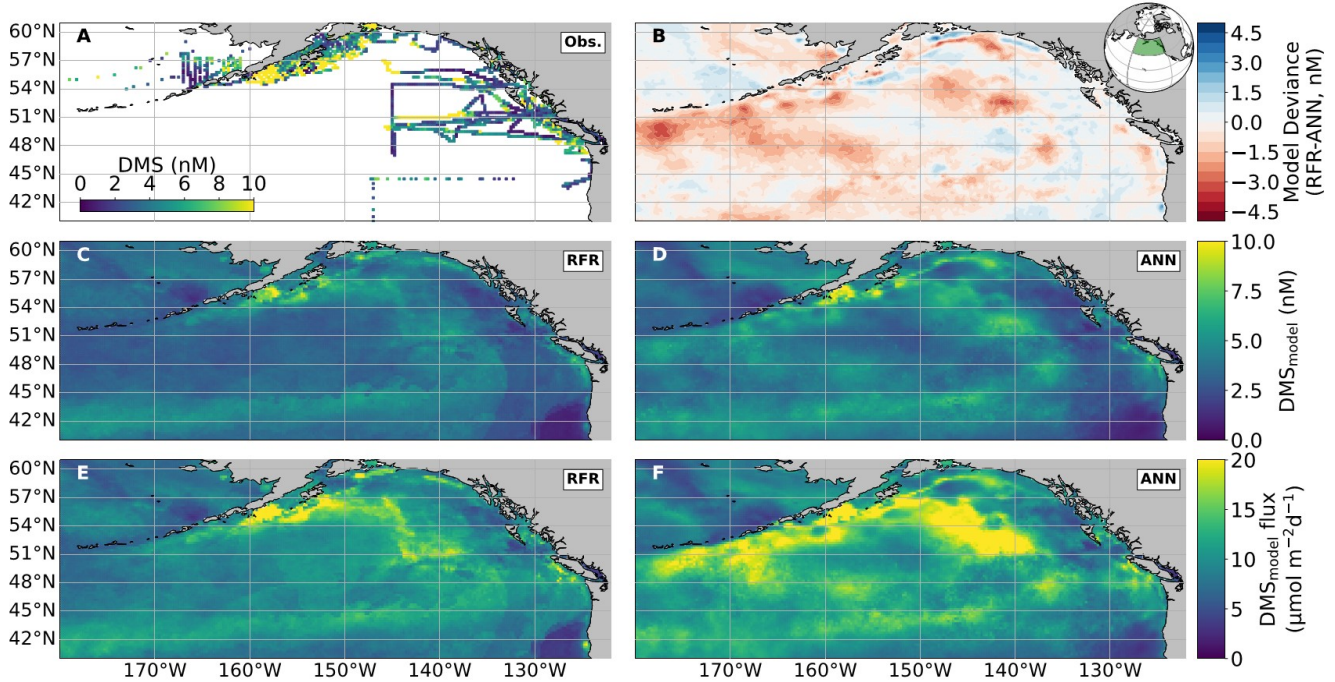
Fig. 4. Predicted maps of sea surface DMS concentrations and sea-air fluxes. (a) Ship-based observations of mean summertime (June-August) DMS concentrations used to construct the predictive models. (b) Differences between the (c) Random Forest Regression (RFR) and (d) Artificial Neural Network (ANN) ensemble predicted DMS concentrations. (e,f) DMS sea-air fluxes derived from the predicted DMS concentrations. Colormap ranges are restricted to illustrate trends, with <1% of DMS data exceeding the colorbar limits. The inset map in (b) shows the NESAP study region as a shaded green patch in a global orthographic projection.

Sea-air DMS fluxes (Fig. 4e,f) derived from ANN predictions were 18% higher, on average, than RFR predictions, largely due to higher predicted values in the Alaska Gyre (Fig. 4d-e, Table 3). The distribution of ANN sea-air fluxes was also closer to ship-based observations (Fig. 5). Predicted regional fluxes ranged from 0.8 to 167 μmol m^{-2} d^{-1} between the two models (Fig. 4e,f, 5), with the highest predicted DMS emissions in August, when derived sea-air fluxes were approximately 1.6 to 2-fold greater than in June and July (Table 3). Our models yielded a summertime integrated sea-air flux of 1.16±1.22 Tg DMS-derived sulfur, which is consistent with the Lana et al. (2011) climatological estimate of 1.64 ± 0.51 Tg (Table 3).

297

298   Table 3. Monthly and mean summertime NESAP sea-air DMS fluxes. Total cumulative fluxes of DMS-derived sulfur (Tg,

299   mean ± SD) are calculated from the Random Forest Regression (RFR) and Artificial Neural Network (ANN) model predictions

300   (based on an ensemble of 2000 models). Total cumulative NESAP sea-air flux derived from the Lana et al. (2011) climatology

301   is shown for comparative purposes.

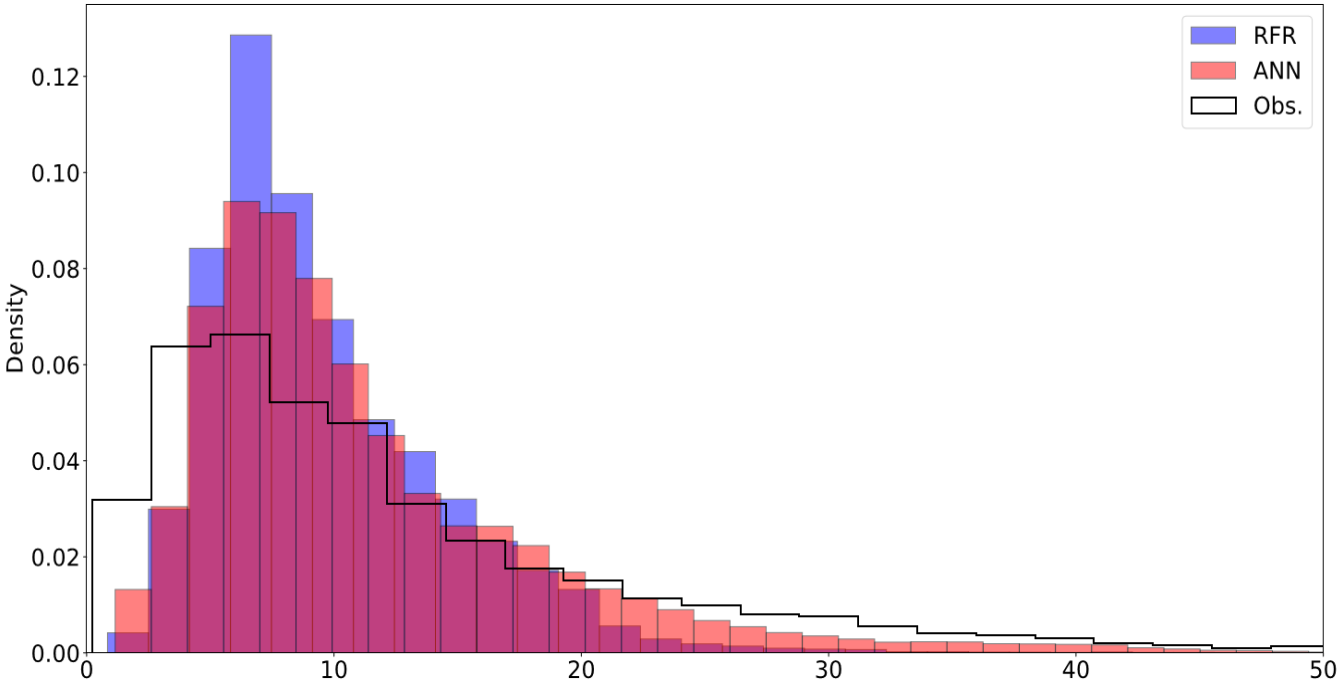|			Summertime Sulfur Emissions	
	RFR	ANN	This Study	Lana et al. (2011)
	$\mu mol\ m^{-2}\ d^{-1}$	$\mu mol\ m^{-2}\ d^{-1}$	Tg S	Tg S
June	8.0 ± 5.3	8.0 ± 5.5	0.29 ± 0.19	0.59 ± 0.24
July	8.2 ± 3.5	9.7 ± 4.6	0.33 ± 0.14	0.41 ± 0.16
August	12.7 ± 3.5	16.5 ± 4.6	0.54 ± 0.25	0.65 ± 0.25
June-August	9.7 ± 2.8	11.4 ± 4.0	1.16 ± 0.35	1.64 ± 0.51

302

303

304

305

306   **Fig. 5. Histograms of DMS sea-air flux distributions derived from the 1000-model ensemble random forest regression (RFR) and**
307   **artificial neural network (ANN) predictions as well as cruise observations (Obs.). The sample sizes of both models are equivalent**
308   **(n= 49,632) and are significantly higher than the observational dataset (n=2063). Note that the distribution is restricted to show**

16

309 **trends, with a maximum flux of 238 nM (Obs.). The upper tail (>50 nM) consists of only 2.9% (Obs.) and <0.1% (both RFR and**
310 **ANN) of the values. Note that the ANN better predicts the upper tail of DMS observations greater than 20 nM.**

311

3.4 Drivers of DMS variability

313 In addition to modelling the spatial and temporal distribution of surface water DMS in the NESAP, we
314 examined the influence of different oceanographic variables as model predictors. As expected based on previous
315 work (Herr et al., 2019), no single predictor was found to exert a dominant control on modelled DMS distributions
316 from either the RFR or ANN models (Fig. 6, 7). Rather, the relationship between DMS and other oceanographic
317 variables exhibited significant region-specific patterns. One of the most compelling regional signatures was the
318 apparent relationship between DMS and SSHA. In both models, we found significant positive correlations between
319 DMS and SSHA (ρ=0.35, 0.42 for RFR and ANN, respectively) across the full spatial domain, with a particularly
320 notable relationship along the northern Alaskan coastline (Fig. 8, 9). Here, strong winds (Fig. 9j-l), coupled with
321 the northeastern Alaska current flow, produce two characteristic oceanographic features in the NESAP: strong,
322 semi-permanent mesoscale eddies collectively referred to as the Haida, Sitka and Yakutat eddies (Fig. 8a), and the
323 formation of the high nutrient, low chlorophyll (HNLC) Alaska Gyre (Fig. 8c; Okkonen et al., 2001; Whitney et
324 al., 2005). Both the monthly (Fig. 9a-i) and summertime-averaged (Fig. 8a,b) RFR and ANN-derived DMS
325 concentrations are low where these downwelling eddies form. In contrast, elevated DMS concentrations were
326 associated with the negative SSHA coastal upwelling areas (Fig. 8a,b), where phytoplankton productivity is
327 stimulated by nutrient inputs into the mixed layer.
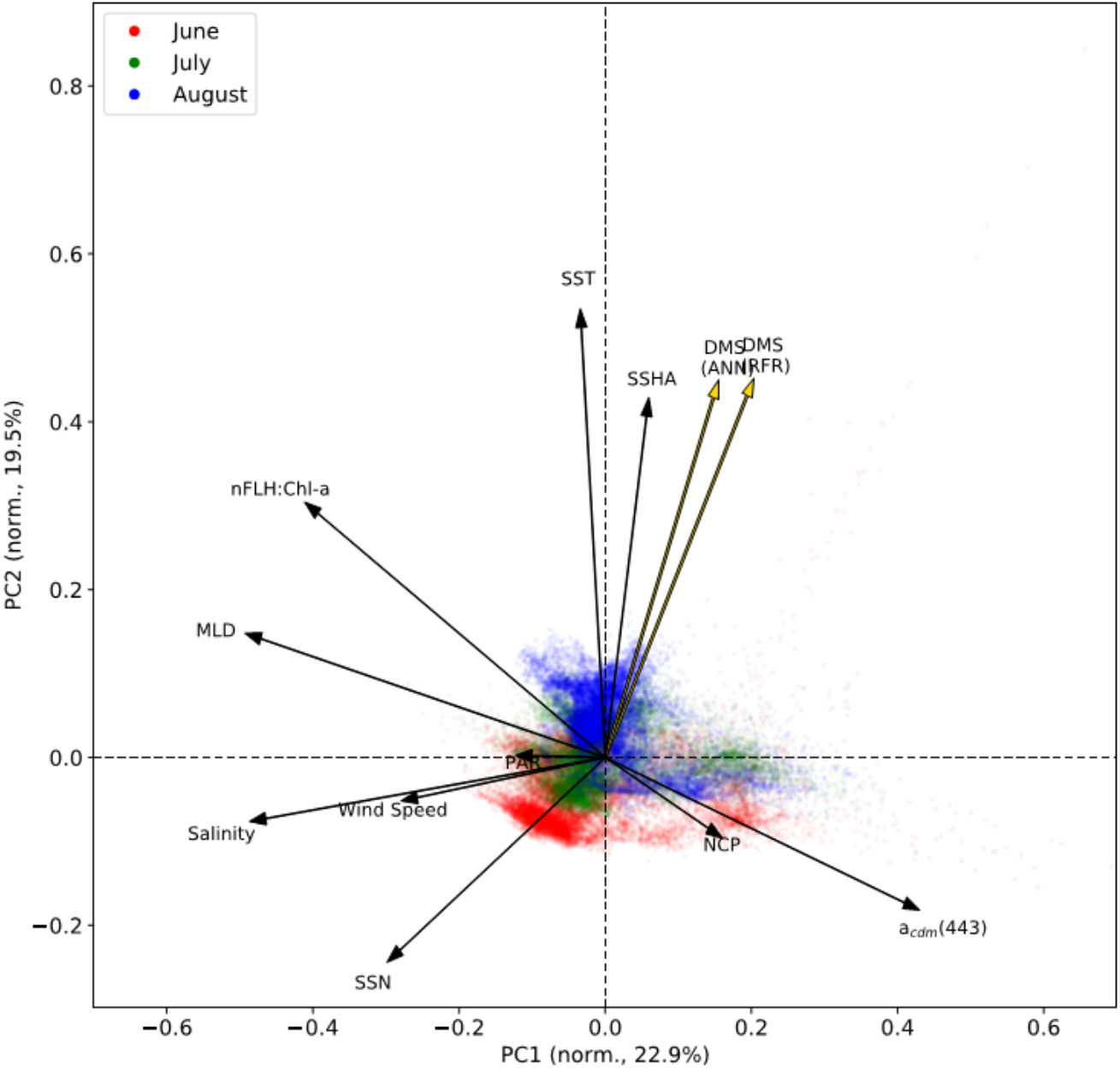
Fig. 6. Principal Component Analysis (PCA) showing the relationships between variables used to construct the predictive algorithms. Eigenvectors (arrows) are superimposed over the principal components (PCs; data points) for the first two significant modes obtained from PCA. PCs are normalized and clustered by month (June-August, see legend for colors), while the eigenvectors are grouped by ensemble model predictions (gold) and nine predictor variables (black). The percentage of variance explained by each mode is indicated along the axes.
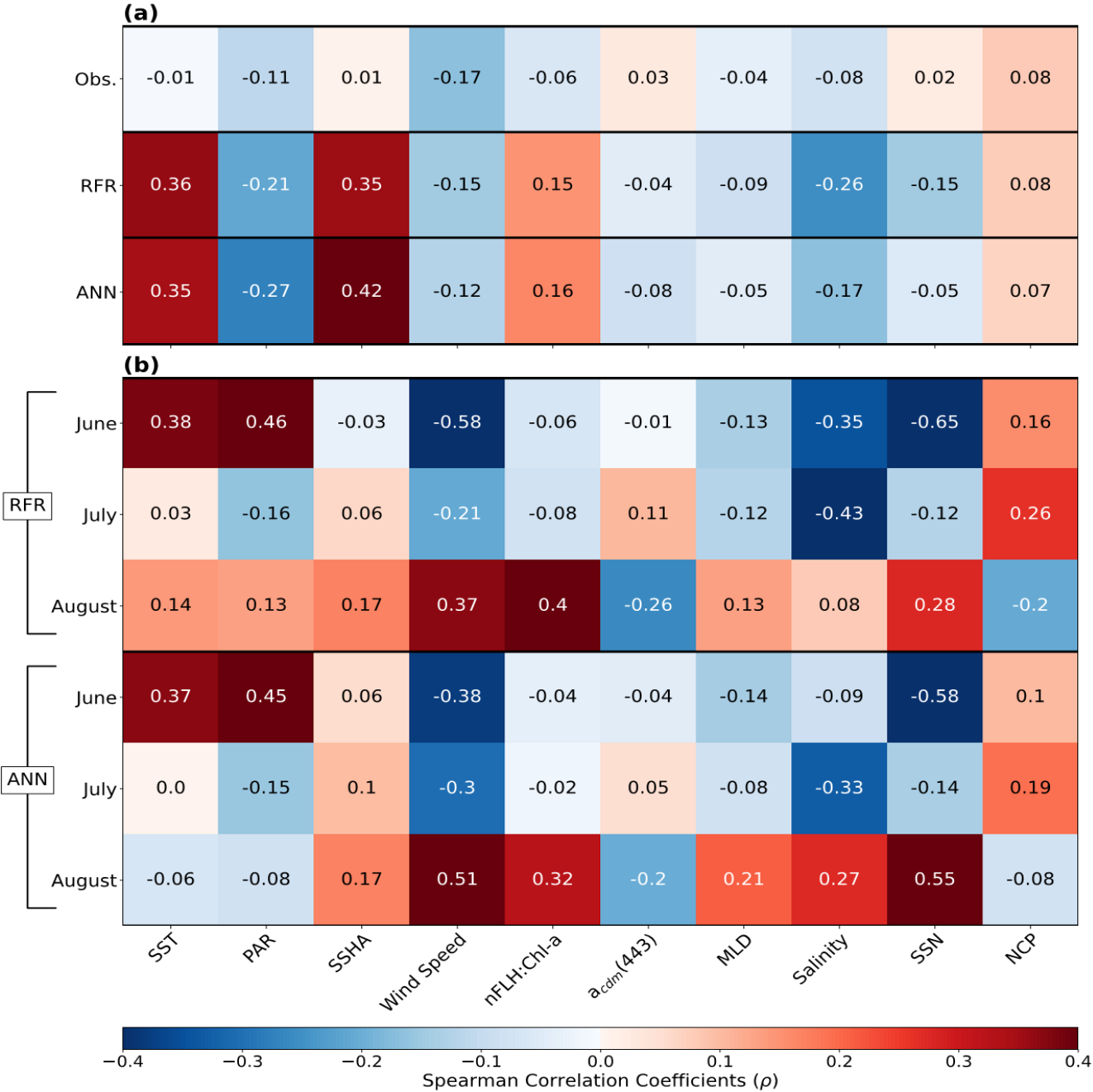
Fig. 7. Heatmap of Spearman rank correlations (ρ). (a) Correlations of pooled data (June-August) for DMS observations (Obs.), RFR and ANN predictions per variable. (b) Correlations per month for the RFR and ANN DMS predictions. All model correlations are computed on the 1000-model ensembles.

340   Modelled DMS concentrations also significantly correlated with hydrographic frontal patterns. We found

341   significant correlations between DMS and SST ($\rho=0.36$, 0.35 for RFR and ANN, respectively) which suggested

342   the central Alaska Gyre and offshore of Vancouver Island are areas of elevated DMS variability (Fig. 8b). Both

343   models predict high DMS levels in the northern frontal zone of the gyre (140°W-145°W) between the 10.5 and

344   12°C isotherms and the southern frontal zone between (42°N-45°N) between the 13.5 and 15°C isotherms (Fig.

345   8b,c). By comparison, our models suggest that DMS concentrations are predominantly low in relation to high sea

346   surface nitrate (SSN) concentrations within the HNLC gyre (Fig. 8, 9). As discussed below, the relationship

347   between DMS and macronutrient concentrations in the HNLC waters of the central Gulf of Alaska could indicate

348   an important role for iron limitation as a controlling factor in the DMS cycle. The presence of elevated summer

349   nutrients in offshore waters is taken as a proxy for iron limitation, which increases over the course of the summer

350   growing season.
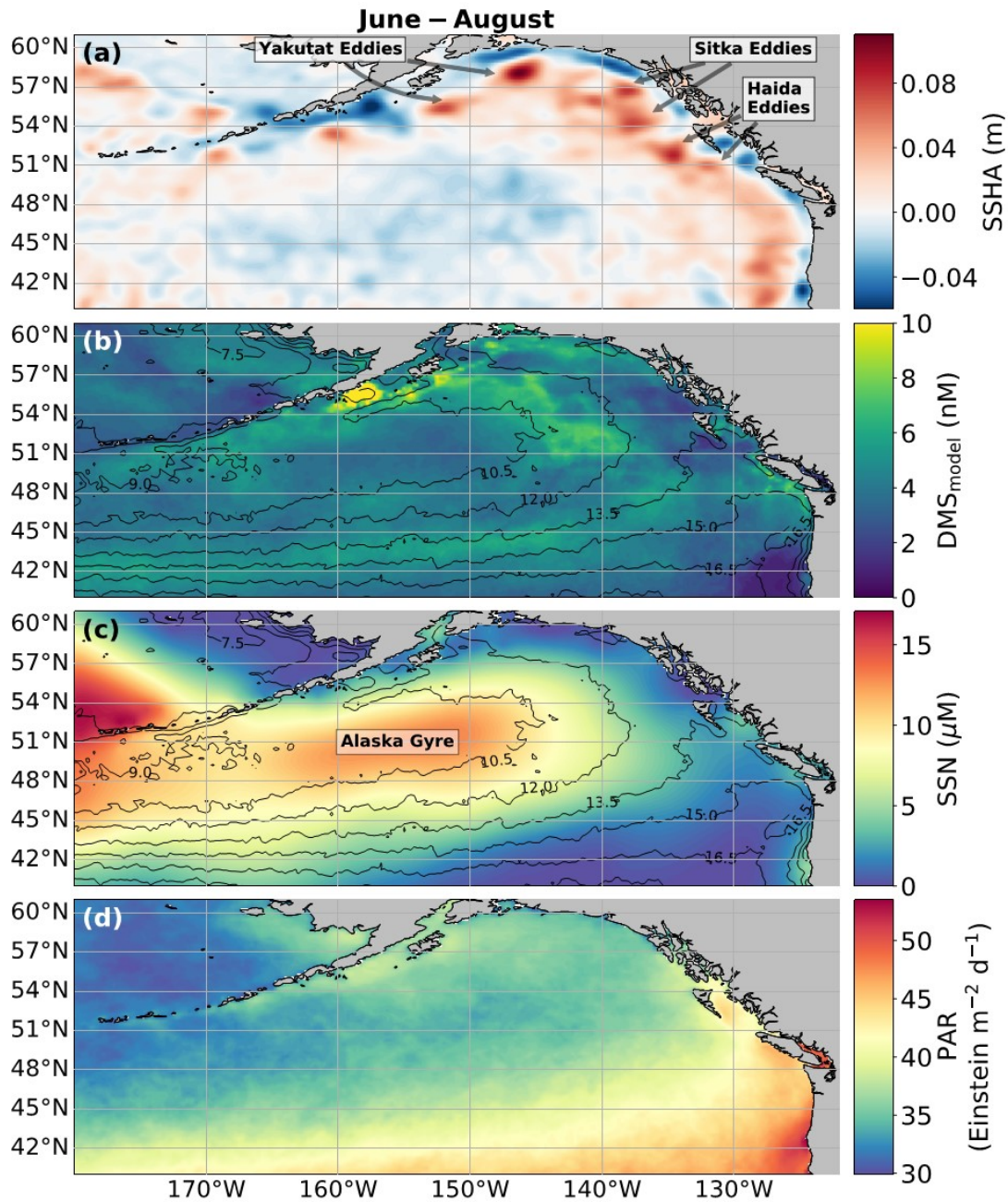
Fig. 8. Physical drivers of summertime (June-August) NESAP DMS distributions. (a) Sea surface height anomalies (SSHA), (b) predicted DMS concentrations derived from the mean of all 2000 RFR and ANN machine learning models, (c) sea surface nitrate (SSN) and (d) photosynthetically active radiation (PAR). Contours in (b,c) show sea surface temperature (SST) isotherms. Coherent features of elevated sea-surface height indicate the presence of mesoscale eddies, whereas nearshore low SSHAs features reveal areas of upwelling. Colormaps ranges are restricted to illustrate trends with <1% of data exceeding the colorbar limits.

358   Other variables appear to exhibit a more localized or minimal influence on DMS cycling. For instance,
359   both NCP and DMS are elevated in productive nearshore waters, but NCP generally correlates weakly with both
360   RFR- and ANN-derived DMS concentrations ($\rho=0.08$, 0.07 for RFR and ANN, respectively). It should be noted,
361   however, the empirically-derived NCP estimates may carry more uncertainty than other predictors obtained from
362   direct satellite observations (Li and Cassar, 2016). Similarly to NCP, modelled phytoplankton taxonomic
363   composition (Hirata et al., 2011; Zeng et al., 2018) was not significantly correlated with predicted DMS
364   concentrations ($\rho<0.1$). Although strong, persistent winds appear to sustain low DMS concentrations off the coast
365   of Oregon and Vancouver Island (Fig. 9), wind speeds only weakly correlate with DMS overall for the region ($\rho=$-
366   0.15 and -0.12 for RFR and ANN, respectively). Additionally, high PAR in these areas correspond with low DMS
367   concentrations (Fig. 6d) and there is an overall negative correlation between PAR and DMS for the region (Fig. 6,
368   7; $\rho=$-0.21 and -0.27 for RFR and ANN, respectively). Finally, despite hypothesized links between DMS cycling
369   and iron limitation in the NESAP (Levasseur et al., 2006; Merzouk et al., 2006; Royer et al., 2010), nFLH:Chl-a
370   ratios (taken as a proxy for phytoplankton iron stress; Behrenfeld et al., 2009; Westberry et al., 2013) did not exhibit
371   any coherent spatial patterns, and only weakly correlated to our modelled DMS concentrations ($\rho=0.15$ and $\rho=0.16$
372   for RFR and ANN, respectively).

373
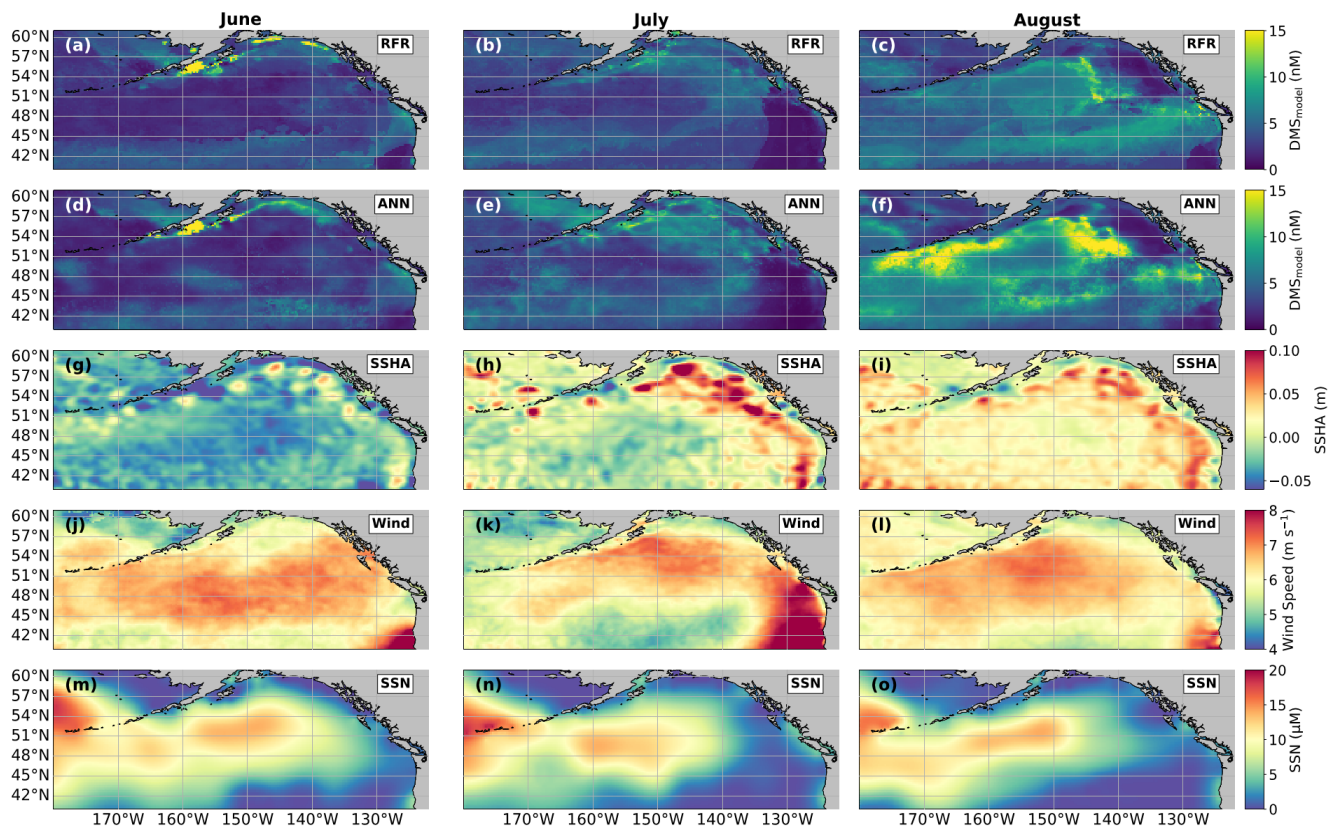
Fig. 9. Predicted spatial and temporal (June-August) DMS distribution in relation to underlying oceanographic variables. DMS concentrations predicted from (a-c) the Random Forest Regression (RFR) and (d-f) the Artificial Neural Network (ANN) ensemble models are mapped alongside the monthly-averaged (g-i) sea surface height anomalies (SSHA), (j-l) wind speeds (Wind), and (m-o) sea surface nitrate (SSN) for each month. Colormap ranges are restricted to illustrate trends, with at most 1.5% of the data beyond the colorbar limits.

4 Discussion

The relative sparsity of DMS data in many oceanic regions and the complexity of DMS cycling have limited previous attempts to model oceanic distributions of this compound (Simó and Dachs, 2002; Vallina and Simó, 2007; Galí et al., 2018; Watanabe et al., 2007; Herr et al., 2019). Taking advantage of expanding data resources, we employed a new approach to statistically describe DMS distributions in the NESAP. Our results show that both our RFR and ANN models substantially improved predictive strength over traditional empirical approaches (Fig. 2, 3), while identifying several key DMS relationships and regional patterns across the NESAP (Fig. 8, 9). Although our statistical approach does not directly elucidate the underlying mechanisms driving these relationships, and not all variability in predictors may be captured at the single spatial scale used here, we can nonetheless make some

23

reasonable inductive inferences. These inferences are discussed below, along with the implications of the improved predictive performance observed here.

4.1 Relationships with other oceanographic variables

Among the more prominent spatial relationships we observed was the coherence between predicted DMS concentrations and SST, and the negative correlation between predicted DMS concentrations and sea surface nitrate (SSN) within and surrounding the Alaska Gyre (Fig. 6-9). Notably, regional SSN, NCP and Chl-a distributions did not vary appreciably inside versus outside the gyre, and these variables were poorly correlated with DMS concentrations (r=-0.02, ρ=0.08 with NCP, r=0.09, ρ=-0.12 with Chl-a). This suggests that the patterns in surface DMS across the Alaska Gyre were not simply driven by changes in phytoplankton biomass or productivity. The DMS-nitrate relationship may be partially explained by the so-called sulfur overflow hypothesis (Stefels, 2000), which suggests that nutrient-limited phytoplankton increase DMSP production and its subsequent cleavage to DMS, in order to regulate intracellular sulfur quotas when protein synthesis is limited (Hatton & Wilson, 2007; Kinsey et al., 2016; Simó & Vila-Costa, 2006; Spiese & Tatarkov, 2014; Stefels, 2000). This mechanism may help explain the higher predicted DMS concentrations at the northern extent of the Alaska Gyre, where SSN concentrations begin to decrease (Fig. 6). Nutrient-dependent effects may also be important in explaining seasonal variability, as the DMS-nitrate relationship becomes positive in August as phytoplankton growth becomes increasingly nutrient limited (Fig. 7b).

The apparent relationship between DMS and nitrate could also result indirectly from the underlying effects of iron limitation. Excess summertime nitrate concentrations are taken as evidence for iron limitation in the NESAP (Boyd and Harrison, 1999; Boyd et al., 2004; Martin and Fitzwater, 1988; Whitney et al., 2005). Under iron-limiting conditions, DMS is thought to function, together with DMSP and DMSO, as part of an antioxidant response to oxidative stress (Sunda et al., 2002). This hypothesis suggests that iron limitation should stimulate net production of DMS and DMSP (Bucciarelli et al., 2013; Sunda et al., 2002), which is inconsistent with the overall negative dependence predicted between DMS and SSN (Fig. 8b,c).

Satellite-based, chlorophyll-normalized fluorescence has been suggested as an additional proxy for iron limitation. Low iron conditions can lead to both a reduction in photosystem I relative to photosystem II (Strzepek and Harrison, 2004), and an apparent increase in energetically-decoupled light harvesting complexes (Allen et al., 2008; Behrenfeld & Milligan, 2013), resulting in elevated fluorescence-to-chlorophyll a ratios (nFLH:Chl-a) (Westberry et al., 2013). To our knowledge, this proxy has not been widely investigated with respect to DMS cycling. In our analysis, we found that nFLH:Chl-a ratios, and the NPQ-corrected fluorescence yields (φ_f), exhibited

only weak positive correlations with the RFR and ANN predicted DMS concentrations (Fig. 6, 7). Moreover, neither of these metrics exhibited coherent spatial patterns with predicted DMS concentrations, suggesting a limited role for iron in driving spatial patterns of DMS cycling within the NESAP. However, it is important to note the potential temporal mismatch between our monthly DMS predictions and these more instantaneous metrics of iron limitation, which reflect short-term physiological changes (days to weeks; Behrenfeld et al., 2009; Westberry et al., 2019) that depend on sporadic iron loading (*e.g.* aerosol deposition; Mahowald et al., 2009). Indeed, both natural and artificial iron-fertilization events have thus far been detected from satellite-derived nFLH:Chl-a at daily resolution (Westberry et al., 2013), in contrast to the monthly-averaged data used here. Therefore, modelling frameworks utilizing shorter temporal scales may find a clearer connection between DMS cycling and iron limitation using the chlorophyll-a fluorescence proxy.

Beyond nutrient limitation effects, ambient light fields are believed to exert significant direct and indirect effects on DMS cycling (del Valle et al., 2007). At the community level, high irradiance may inhibit bacterial consumption of DMS (Slezak et al., 2001; Toole et al., 2006; Lizotte et al., 2012), while covarying changes in mixing and high irradiance can induce transient selectivity for high-light acclimated species and influence the proportion of high DMS/P producers within assemblages (Galí et al., 2013; Vance et al., 2013). Ultraviolet radiation has been noted to induce high DMS production and turnover through a proposed cascading oxidation pathway, which acts to remove harmful reactive oxygen species (Sunda et al., 2002; Archer et al., 2010). In contrast, more recent evidence has indicated the potential for elevated DMS production in the NESAP from the reduction of DMSO due to light-induced oxidative stress over diurnal cycles (Herr et al., 2020). Although our modelled DMS concentrations exhibited an overall negative correlation with PAR (Fig. 6, 7a), monthly correlations indicate a stronger positive correlation between DMS and PAR in June, where the summer solstice drives high irradiance. In contrast, July and August exhibit much weaker negative correlations as the summer bloom declines (Fig. 7b). These results provide indirect evidence that light-induced oxidative stress, possibly coupled with inhibition of microbial DMS consumption, may influence regional NESAP DMS distributions, particularly early in the summer.

The overall negative association of DMS and incident light (Fig. 6,7a) may also indicate a role for photolysis in DMS loss through (del Valle et al., 2007). Since DMS does not have strong light absorption properties, the presence of photosensitisers is necessary for the abiotic photooxidation of DMS (Brimblecombe and Shooter, 1986). To account for this process, our models incorporated nitrate (SSN) and $a_{cdm}(443)$ (as a proxy for CDOM; Nelson & Siegel, 2013), both of which are thought to be dominant photosensitisers of DMS in marine systems (Taalba et al., 2013; Bouillon and Miller, 2004, 2005; Galí et al., 2016). In the NESAP, nitrate appears to exert a stronger influence than CDOM on the apparent quantum yields (AQY) of DMS (Bouillon and Miller, 2004). In

25

450 support of this, our results suggest a stronger negative dependence of predicted DMS concentrations on nitrate

451 compared to CDOM within the NESAP, particularly in June when irradiance is high (Fig. 6, 7). We acknowledge,

452 however, that the DMS-nitrate relationship likely also reflects physiological impacts of nutrient limitation, as

453 discussed above. Nonetheless, our results are consistent with elevated rates of DMS photo-oxidation in the nitrate-

454 replete, low iron waters of the Alaska Gyre, where photolysis may drive strong DMS oxidation and explain the low

455 predicted DMS concentrations (Fig. 8, 9). Further *in situ* work will be required to resolve the relative contributions

456 of these biotic and abiotic processes to DMS cycling within these areas.

457   Among all the statistical relationships we observed, perhaps the most striking was the association of DMS

458 variability with SSHA, particularly along the Alaskan coast and in relation to mesoscale eddies (Okkonen et al.,

459 2001; Whitney et al., 2005; Fig. 8, 9). To our knowledge, only one other study has linked SSHA to DMS within

460 the NESAP. Herr et al., (2019) demonstrated contrasting positive and negative correlations between DMS and

461 SSHA in offshore and coastal waters, respectively, in general agreement with our results. Presently, the underlying

462 mechanisms explaining the relationship between SSHA and DMS cycling remain unclear, yet it is likely that

463 physical mixing processes are important. For example, enhanced biological production is known to be stimulated

464 by eddy re-supply of iron and macronutrients via vertical advection and diffusion (Whitney et al., 2005; Bailey et

465 al., 2008). These nutrient supply processes would also be expected to influence DMS cycling, as outlined above.

466 Elevated abundances of high DMS-producers within anticyclonic eddies with positive sea surface height anomalies

467 have been noted in the Sargasso Sea (Bailey et al., 2008), while eddy-induced vertical transport likely supplements

468 nearshore, current-driven upwelling that can also resupply iron into the coastal waters of the NESAP (Cullen et al.,

469 2009; Freeland et al., 1984). In addition, eddy propagation can allow cross-shelf transport, distributing

470 micronutrients to offshore waters (Fiechter and Moore, 2012), potentially contributing to the apparent elevated

471 DMS concentrations in the outer Alaska gyre between the 10.5 and 12°C isotherms (Fig. 8). These mixing and

472 transport mechanisms could partially explain the influence of elevated productivity in driving increased nearshore

473 and northern NESAP DMS concentrations (Fig. 4, 7-9), representing a novel source of DMS variability in this

474 region.

475   The taxonomic composition of plankton assemblages is also a likely source of variability influencing DMS

476 cycling. Significant changes to DMS production and consumption rates within the NESAP are expected in response

477 to variable microbial and phytoplankton taxonomy (Vila-Costa et al., 2006; Lidbury et al., 2016; Sheehan and

478 Petrou, 2020). Such taxonomic variability may, in turn, reflect transient community composition shifts in response

479 to mixing (Bailey et al., 2008), nitrate (Bouillon and Miller, 2004), and iron availability (Levasseur et al., 2006;

480 Merzouk et al., 2006). The monthly averaging used in our data processing removes autocorrelation associated with

481 individual sampling expeditions (Wang et al., 2020), but it may preclude capturing these transient taxonomic

482 responses. For instance, coccolithophores are believed to influence DMS cycling in the NESAP (Herr et al., 2019;

483 Asher et al., 2011), yet monthly-averaged calcite distributions did not yield increased predictive strength for DMS

484 concentrations in our analysis (see Sect. 2.6). However, as satellite PIC preferentially reflects the optical signature

485 of detached coccoliths, monthly-averaged satellite PIC observations may represent the senescence of

486 coccolithophore blooms, rather than active growth phases. Additionally, applying a chlorophyll-a based taxonomic

487 algorithm (Hirata et al., 2011; Zeng et al., 2018) yielded no further explanation of the DMS variability predicted.

488 The influence of taxonomic composition thus remains cryptic within our modelling framework.

489 **4.2 Implications of Improved Predictive Power**

490 As noted above, both the RFR and ANN approaches demonstrate significantly improved accuracy over

491 existing models, explaining up to 62% of observed DMS variability (Fig. 2, 3). This predictive skill is somewhat

492 lower than that achieved for methane fluxes (Weber et al., 2019) and dissolved inorganic carbon dynamics (Roshan

493 and DeVries, 2017), where R^2 values ranging from 0.7 to 0.95 were obtained. Nonetheless, the dramatic accuracy

494 improvement of our algorithms over traditional methods (Fig. 2, 3) encourages the further use of these techniques

495 in modelling DMS distributions.

496 Improved predictive accuracy provides opportunities to gain insight into the mechanisms driving DMS cycling.

497 Our approach has yielded accurate DMS predictions at a 4 to 40-fold higher resolution then previous algorithms

498 (Simó and Dachs, 2002; Vallina and Simó, 2007; Galí et al., 2018; Watanabe et al., 2007), enabling the description

499 of mesoscale patterns and processes (Fig. 8). Extending these methods to sub-mesoscale resolution will enable

500 investigations into the dependence of DMS on finer-scale hydrographic processes, particularly stratification and

501 frontal dynamics, which have been increasingly linked to DMS cycling but remain unresolved mechanistically

502 (Royer et al., 2015; Asher et al., 2011). Moreover, coupling machine learning algorithms with biophysical and

503 tracer export models holds promise to resolve the contributions of eddy dynamics and upwelling intensity on DMS

504 variability, likely through nutrient availability and physiological mechanisms (Asher et al., 2011; Bailey et al.,

505 2008; Cullen et al., 2009). Recent work has also developed a new database of DMS apparent quantum yields (Galí

506 et al., 2016). As the availability of these measurements increases, simultaneous mapping of both DMS quantum

507 yields and concentrations will become feasible, enabling future studies to better parse out the contribution of

508 photolysis, physical mixing, and biological drivers of DMS cycling.

509 Although used in a diagnostic capacity here, our statistical models also hold potential for prognostic

510 applications. Frameworks utilizing shorter time scales will likely be able to detect underlying mechanisms

driving observed diel cycling (Galí et al., 2013; Royer et al., 2016), even if the underlying mechanisms are still unresolved. We note, however, that caution will need be exercised as machine learning models have a tendency to overfit noise (Weber et al., 2019; Roshan and DeVries, 2017; Wang et al., 2020), thus requiring appropriately large training datasets and the use of known "future" observations to validate predictive accuracy in this context. The significant variability in DMS cycling across oceanic regimes will likely also render predictions more successful at regional, rather than global, scales (Galí et al., 2018; Royer et al., 2015). Nonetheless, prognostic applications of these algorithms should be investigated to aid in the future development of improved mechanistic models.

5 Conclusions

We have presented a statistical approach for modelling DMS distributions, which provides significantly higher predictive skill than traditional methods (Simó and Dachs, 2002; Vallina and Simó, 2007; Galí et al., 2018; Watanabe et al., 2007; Lana et al., 2011), and yields estimates of the summertime NESAP DMS sea-air fluxes to 1.16±1.22 Tg S in agreement with previous findings (Herr et al., 2019; Lana et al., 2011). Our results further underscore the importance of the NESAP to global DMS production and motivate further observations in traditionally under-sampled areas such as the Alaska Gyre and Aleutian Islands. Although we are unable to directly examine the mechanistic drivers of DMS variability, our findings suggest nutrient limitation, light-driven processes, and eddy-induced mixing are potentially key drivers of DMS cycling in the NESAP. Future studies will benefit from using such statistical algorithms, in conjunction with field-based process studies and mechanistic models, to better understand the underlying dynamics and driving factors in the oceanic DMS cycle.

Code availability. The analysis in this study makes extensive use of the Numpy, Matplotlib, & Scikit-Learn libraries in Python. The custom codes used can be downloaded at https://github.com/bjmcnabb/DMS_Climatology/tree/main/NESAP or are available upon request from the corresponding author.

Data Availability. DMS observations and predictor datasets are described in the Methods with relevant links to repositories. Data from the Lana et al. (2011) climatology used for comparison in Table 3 are available via the SOLAs project (retrieved from www.bodc.ac.uk/solas_integration/implementation_products/group1/dms/), where the DMS sea-air fluxes were calculated as described in Sect. 2.3. The gridded climatologies produced from each

538 algorithm in this study can be obtained at
539 https://github.com/bjmcnabb/DMS_Climatology/tree/main/NESAP/Climatologies.

546

References

Allen, A. E., LaRoche, J., Maheswari, U., Lommer, M., Schauer, N., Lopez, P. J., Finazzi, G., Fernie, A. R., and Bowler, C.: Whole-cell response of the pennate diatom Phaeodactylum tricornutum to iron starvation, Proceedings of the National Academy of Sciences, 105, 10438–10443, https://doi.org/10/cs9k8x, 2008.

Archer, S. D., Ragni, M., Webster, R., Airs, R. L., and Geider, R. J.: Dimethyl sulfoniopropionate and dimethyl sulfide production in response to photoinhibition in Emiliania huxleyi, Limnology and Oceanography, 55, 1579–1589, https://doi.org/10/dvpwqb, 2010.

Asher, E. C., Merzouk, A., and Tortell, P. D.: Fine-scale spatial and temporal variability of surface water dimethylsulfide (DMS) concentrations and sea–air fluxes in the NE Subarctic Pacific, Marine Chemistry, 126, 63–75, https://doi.org/10/chmbhk, 2011.

Asher, E. C., Dacey, J. W., Ianson, D., Peña, A., and Tortell, P. D.: Concentrations and cycling of DMS, DMSP, and DMSO in coastal and offshore waters of the Subarctic Pacific during summer, 2010-2011, J. Geophys. Res. Oceans, 122, 3269–3286, https://doi.org/10.1002/2016JC012465, 2017.

Ayers, G. P. and Cainey, J. M.: The CLAW hypothesis: a review of the major developments, Environ. Chem., 4, 366, https://doi.org/10/b7p54b, 2007.

Bailey, K. E., Toole, D. A., Blomquist, B., Najjar, R. G., Huebert, B., Kieber, D. J., Kiene, R. P., Matrai, P., Westby, G. R., and del Valle, D. A.: Dimethylsulfide production in Sargasso Sea eddies, Deep Sea Research Part II: Topical Studies in Oceanography, 55, 1491–1504, https://doi.org/10/fnqb6j, 2008.

Bates, T. S., Lamb, B. K., Guenther, A., Dignon, J., and Stoiber, R. E.: Sulfur emissions to the atmosphere from natural sources, J Atmos Chem, 14, 315–337, https://doi.org/10/chmgt6, 1992.

Behrenfeld, M. J. and Falkowski, P. G.: Photosynthetic rates derived from satellite-based chlorophyll concentration, Limnology and Oceanography, 42, 1–20, https://doi.org/10/cg5x4k, 1997.

Behrenfeld, M. J. and Milligan, A. J.: Photophysiological Expressions of Iron Stress in Phytoplankton, Annu. Rev. Mar. Sci., 5, 217–246, https://doi.org/10.1146/annurev-marine-121211-172356, 2013.

Behrenfeld, M. J., Westberry, T. K., Boss, E. S., O'Malley, R. T., Siegel, D. A., Wiggert, J. D., Franz, B. A., McClain, C. R., Feldman, G. C., Doney, S. C., Moore, J. K., Dall'Olmo, G., Milligan, A. J., Lima, I., and Mahowald, N.: Satellite-detected fluorescence reveals global physiology of ocean phytoplankton, Biogeosciences, 6, 16, https://doi.org/10/fdn3f2, 2009.

Bell, T. G., De Bruyn, W., Miller, S. D., Ward, B., Christensen, K. H., and Saltzman, E. S.: Air–sea dimethylsulfide (DMS) gas transfer in the North Atlantic: evidence for limited interfacial gas exchange at high wind speed, Atmos. Chem. Phys., 13, 11073–11087, https://doi.org/10.5194/acp-13-11073-2013, 2013.

Belviso, S., Sciandra, A., and Copin-Montégut, C.: Mesoscale features of surface water DMSP and DMS concentrations in the Atlantic Ocean off Morocco and in the Mediterranean Sea, Deep Sea Research Part I: Oceanographic Research Papers, 50, 543–555, https://doi.org/10.1016/S0967-0637(03)00032-3, 2003.

581 Blomquist, B. W., Brumer, S. E., Fairall, C. W., Huebert, B. J., Zappa, C. J., Brooks, I. M., Yang, M., Bariteau,
582 L., Prytherch, J., Hare, J. E., Czerski, H., Matei, A., and Pascal, R. W.: Wind Speed and Sea State Dependencies
583 of Air-Sea Gas Transfer: Results From the High Wind Speed Gas Exchange Study (HiWinGS), 122, 8034–8062,
584 https://doi.org/10/gcmxd3, 2017.

585 Bock, J., Michou, M., Nabat, P., Abe, M., Mulcahy, J. P., Olivié, D. J. L., Schwinger, J., Suntharalingam, P.,
586 Tjiputra, J., van Hulten, M., Watanabe, M., Yool, A., and Séférian, R.: Evaluation of ocean dimethylsulfide
587 concentration and emission in CMIP6 models, Biogeosciences, 18, 3823–3860, https://doi.org/10/gk6fw8, 2021.

588 Bouillon, R.-C. and Miller, W. L.: Determination of apparent quantum yield spectra of DMS photo-degradation
589 in an in situ iron-induced Northeast Pacific Ocean bloom: AQY of DMS in an iron-induced bloom, Geophys.
590 Res. Lett., 31, n/a-n/a, https://doi.org/10/d96wkn, 2004.

591 Bouillon, R.-C. and Miller, W. L.: Photodegradation of Dimethyl Sulfide (DMS) in Natural Waters: Laboratory
592 Assessment of the Nitrate-Photolysis-Induced DMS Oxidation, Environ. Sci. Technol., 39, 9471–9477,
593 https://doi.org/10/d2j84c, 2005.

594 Boyd, P. and Harrison, P. J.: Phytoplankton dynamics in the NE subarctic Pacific, Deep Sea Research Part II:
595 Topical Studies in Oceanography, 46, 2405–2432, https://doi.org/10/fkg4mz, 1999.

596 Boyd, P. W., Law, C. S., Wong, C. S., Nojiri, Y., Tsuda, A., Levasseur, M., Takeda, S., Rivkin, R., Harrison, P.
597 J., Strzepek, R., Gower, J., McKay, R. M., Abraham, E., Arychuk, M., Barwell-Clarke, J., Crawford, W.,
598 Crawford, D., Hale, M., Harada, K., Johnson, K., Kiyosawa, H., Kudo, I., Marchetti, A., Miller, W., Needoba, J.,
599 Nishioka, J., Ogawa, H., Page, J., Robert, M., Saito, H., Sastri, A., Sherry, N., Soutar, T., Sutherland, N., Taira,
600 Y., Whitney, F., Wong, S.-K. E., and Yoshimura, T.: The decline and fate of an iron-induced subarctic
601 phytoplankton bloom, Nature, 428, 549–553, https://doi.org/10/fkgnf4, 2004.

602 Brieman, L.: Random Forests, 45, 5–32, 2001.

603 Brimblecombe, P. and Shooter, D.: Photo-oxidation of dimethylsulphide in aqueous solution, Marine Chemistry,
604 19, 343–353, https://doi.org/10/bqwpc9, 1986.

605 Bucciarelli, E., Ridame, C., Sunda, W. G., Dimier-Hugueney, C., Cheize, M., and Belviso, S.: Increased
606 intracellular concentrations of DMSP and DMSO in iron-limited oceanic phytoplankton Thalassiosira oceanica
607 and Trichodesmium erythraeum, Limnology and Oceanography, 58, 1667–1679,
608 https://doi.org/10.4319/lo.2013.58.5.1667, 2013.

609 Byrd, R. H., Lu, P., Nocedal, J., and Zhu, C.: A Limited Memory Algorithm for Bound Constrained
610 Optimization, SIAM J. Sci. Comput., 16, 1190–1208, https://doi.org/10/bpjm24, 1995.

611 Charlson, R. J., Lovelock, J. E., Andreae, M. O., and Warren, S. G.: Oceanic phytoplankton, atmospheric
612 sulphur, cloud albedo and climate, Nature, 326, 655–661, https://doi.org/10.1038/326655a0, 1987.

613 Cullen, J. T., Chong, M., and Ianson, D.: British Columbian continental shelf as a source of dissolved iron to the
614 subarctic northeast Pacific Ocean, Global Biogeochem. Cycles, 23, https://doi.org/10/b489x8, 2009.

Dacey, J. W. H. and Wakeham, S. G.: Oceanic Dimethylsulfide: Production During Zooplankton Grazing on Phytoplankton, Science, 233, 1314–1316, https://doi.org/10.1126/science.233.4770.1314, 1986.

Dickson, D. M. J. and Kirst, G. O.: Osmotic Adjustment in Marine Eukaryotic Algae: The Role of Inorganic Ions, Quaternary Ammonium, Tertiary Sulphonium and Carbohydrate Solutes, New Phytologist, 106, 645–655, https://doi.org/10.1111/j.1469-8137.1987.tb00165.x, 1987.

Fiechter, J. and Moore, A. M.: Iron limitation impact on eddy-induced ecosystem variability in the coastal Gulf of Alaska, Journal of Marine Systems, 92, 1–15, https://doi.org/10/bvqv4d, 2012.

Franklin, D., Steinke, M., Young, J., Probert, I., and Malin, G.: Dimethylsulphoniopropionate (DMSP), DMSP-lyase activity (DLA) and dimethylsulphide (DMS) in 10 species of coccolithophore, Mar. Ecol. Prog. Ser., 410, 13–23, https://doi.org/10/fk7hmj, 2010.

Freeland, H. J., Crawford, W. R., and Thomson, R. E.: Currents along the pacific coast of Canada, Atmosphere-Ocean, 22, 151–172, https://doi.org/10.1080/07055900.1984.9649191, 1984.

Galí, M., Simó, R., Vila-Costa, M., Ruiz-González, C., Gasol, J. M., and Matrai, P.: Diel patterns of oceanic dimethylsulfide (DMS) cycling: Microbial and physical drivers, Global Biogeochem. Cycles, 27, 620–636, https://doi.org/10.1002/gbc.20047, 2013.

Galí, M., Kieber, D. J., Romera-Castillo, C., Kinsey, J. D., Devred, E., Pérez, G. L., Westby, G. R., Marrasé, C., Babin, M., Levasseur, M., Duarte, C. M., Agustí, S., and Simó, R.: CDOM Sources and Photobleaching Control Quantum Yields for Oceanic DMS Photolysis, Environ. Sci. Technol., 50, 13361–13370, https://doi.org/10/f9jg2w, 2016.

Galí, M., Levasseur, M., Devred, E., Simó, R., and Babin, M.: Sea-surface dimethylsulfide (DMS) concentration from satellite data at global and regional scales, Biogeosciences, 15, 3497–3519, https://doi.org/10/gdrm6n, 2018.

Garcia, H. E., Weathers, K. W., Paver, C. R., Smolyar, I., Boyer, T. P., Locarnini, M. M., Zweng, M. M., Mishonov, A. V., Baranova, O. K., and Seidov, D.: World Ocean Atlas 2018. Vol. 4: Dissolved Inorganic Nutrients (phosphate, nitrate and nitrate+ nitrite, silicate), 35pp., 2019.

Gardner, M. W. and Dorling, S. R.: Artificial neural networks (the multilayer perceptron)—a review of applications in the atmospheric sciences, Atmospheric Environment, 32, 2627–2636, https://doi.org/10/ft4hjb, 1998.

Goddijn-Murphy, L., Woolf, D. K., and Marandino, C.: Space-based retrievals of air-sea gas transfer velocities using altimeters: Calibration for dimethyl sulfide, 117, https://doi.org/10/gm8ngj, 2012.

Green, D. H., Shenoy, D. M., Hart, M. C., and Hatton, A. D.: Coupling of Dimethylsulfide Oxidation to Biomass Production by a Marine Flavobacterium, Appl. Environ. Microbiol., 77, 3137–3140, https://doi.org/10/cp6r33, 2011.

Hatton, A. D. and Wilson, S. T.: Particulate dimethylsulphoxide and dimethylsulphoniopropionate in phytoplankton cultures and Scottish coastal waters, Aquat. Sci., 69, 330–340, https://doi.org/10/dbxk6n, 2007.

Hatton, A. D., Shenoy, D. M., Hart, M. C., Mogg, A., and Green, D. H.: Metabolism of DMSP, DMS and DMSO by the cultivable bacterial community associated with the DMSP-producing dinoflagellate Scrippsiella trochoidea, Biogeochemistry, 110, 131–146, https://doi.org/10/ggnh23, 2012.

Hegg, D. A., Radke, L. F., and Hobbs, P. V.: Measurements of Aitken nuclei and cloud condensation nuclei in the marine atmosphere and their relation to the DMS-Cloud-climate hypothesis, J. Geophys. Res. Atmos., 96, 18727–18733, https://doi.org/10/d6fwx9, 1991.

Herr, A. E., Kiene, R. P., Dacey, J. W. H., and Tortell, P. D.: Patterns and drivers of dimethylsulfide concentration in the northeast subarctic Pacific across multiple spatial and temporal scales, Biogeosciences, 16, 1729–1754, https://doi.org/10.5194/bg-16-1729-2019, 2019.

Herr, A. E., Dacey, J. W. H., Kiene, R. P., McCulloch, R. D., Schuback, N., and Tortell, P. D.: Potential roles of dimethysulfoxide in regional sulfur cycling and phytoplankton physiological ecology in the NE Subarctic Pacific, Limnology and Oceanography, https://doi.org/10/ghfstm, 2020.

Hirata, T., Hardman-Mountford, N. J., Brewin, R. J. W., Aiken, J., Barlow, R., Suzuki, K., Isada, T., Howell, E., Hashioka, T., Noguchi-Aita, M., and Yamanaka, Y.: Synoptic relationships between surface Chlorophyll-a and diagnostic pigments specific to phytoplankton functional types, Biogeosciences, 8, 311–327, https://doi.org/10.5194/bg-8-311-2011, 2011.

Humphries, G. R. W., Deal, C. J., Elliott, S., and Huettmann, F.: Spatial predictions of sea surface dimethylsulfide concentrations in the high arctic, Biogeochemistry, 110, 287–301, https://doi.org/10/fx778z, 2012.

Kiene, R. P. and Linn, L. J.: The fate of dissolved dimethylsulfoniopropionate (DMSP) in seawater: Tracer studies using 35S-DMSP, Geochimica et Cosmochimica Acta, 64, 2797–2810, https://doi.org/10.1016/S0016-7037(00)00399-9, 2000.

Kinsey, J. D., Kieber, D. J., and Neale, P. J.: Effects of iron limitation and UV radiation on Phaeocystis antarctica growth and dimethylsulfoniopropionate, dimethylsulfoxide and acrylate concentrations, Environ. Chem., 13, 195–211, https://doi.org/10.1071/EN14275, 2016.

Kirst, G. O., Thiel, C., Wolff, H., Nothnagel, J., Wanzek, M., and Ulmke, R.: Dimethylsulfoniopropionate (DMSP) in icealgae and its possible biological role, Marine Chemistry, 35, 381–388, https://doi.org/10.1016/S0304-4203(09)90030-5, 1991.

Korhonen, H., Carslaw, K. S., Spracklen, D. V., Mann, G. W., and Woodhouse, M. T.: Influence of oceanic dimethyl sulfide emissions on cloud condensation nuclei concentrations and seasonality over the remote Southern Hemisphere oceans: A global model study, J. Geophys. Res. Atmos., 113, https://doi.org/10/cfrz46, 2008.

Ksionzek, K. B., Lechtenfeld, O. J., McCallister, S. L., Schmitt-Kopplin, P., Geuer, J. K., Geibert, W., and Koch, B. P.: Dissolved organic sulfur in the ocean: Biogeochemistry of a petagram inventory, Science, 354, 456–459, https://doi.org/10.1126/science.aaf7796, 2016.

683 Lana, A., Bell, T. G., Simó, R., Vallina, S. M., Ballabrera-Poy, J., Kettle, A. J., Dachs, J., Bopp, L., Saltzman, E.
684 S., Stefels, J., Johnson, J. E., and Liss, P. S.: An updated climatology of surface dimethlysulfide concentrations
685 and emission fluxes in the global ocean, Global Biogeochem. Cycles, 25, https://doi.org/10/dbqjrm, 2011.

686 Levasseur, M., Scarratt, M. G., Michaud, S., Merzouk, A., Wong, C. S., Arychuk, M., Richardson, W., Rivkin, R.
687 B., Hale, M., Wong, E., Marchetti, A., and Kiyosawa, H.: DMSP and DMS dynamics during a mesoscale iron
688 fertilization experiment in the Northeast Pacific-Part I: Temporal and vertical distributions, Deep Sea Research
689 Part II: Topical Studies in Oceanography, 53, 2353–2369, https://doi.org/10.1016/j.dsr2.2006.05.023, 2006.

690 Li, Z. and Cassar, N.: Satellite estimates of net community production based on O_2/Ar observations and
691 comparison to other estimates, Global Biogeochem. Cycles, 30, 735–752, https://doi.org/10/f8v6bh, 2016.

692 Lidbury, I., Kröber, E., Zhang, Z., Zhu, Y., Murrell, J. C., Chen, Y., and Schäfer, H.: A mechanism for bacterial
693 transformation of dimethylsulfide to dimethylsulfoxide: a missing link in the marine organic sulfur cycle,
694 Enviorn. Microbiol., 18, 2754–2766, https://doi.org/10.1111/1462-2920.13354, 2016.

695 Lizotte, M., Levasseur, M., Michaud, S., Scarratt, M. G., Merzouk, A., Gosselin, M., Pommier, J., Rivkin, R. B.,
696 and Kiene, R. P.: Macroscale patterns of the biological cycling of dimethylsulfoniopropionate (DMSP) and
697 dimethylsulfide (DMS) in the Northwest Atlantic, Biogeochemistry, 110, 183–200, https://doi.org/10/fx9svt,
698 2012.

699 Mahowald, N. M., Engelstaedter, S., Luo, C., Sealy, A., Artaxo, P., Benitez-Nelson, C., Bonnet, S., Chen, Y.,
700 Chuang, P. Y., Cohen, D. D., Dulac, F., Herut, B., Johansen, A. M., Kubilay, N., Losno, R., Maenhaut, W.,
701 Paytan, A., Prospero, J. M., Shank, L. M., and Siefert, R. L.: Atmospheric Iron Deposition: Global Distribution,
702 Variability, and Human Perturbations, Annu. Rev. Mar. Sci., 1, 245–278, https://doi.org/10/fsn8tj, 2009.

703 Malin, G., Wilson, W. H., Bratbak, G., Liss, P. S., and Mann, N. H.: Elevated production of dimethylsulfide
704 resulting from viral infection of cultures of Phaeocystis pouchetii, Limnology and Oceanography, 43, 1389–1393,
705 https://doi.org/10/bw7vjf, 1998.

706 Martin, J. H. and Fitzwater, S. E.: Iron deficiency limits phytoplankton growth in the north-east Pacific subarctic,
707 Nature, 331, 341–343, https://doi.org/10/bvtg6v, 1988.

708 Merzouk, A., Levasseur, M., Scarratt, M. G., Michaud, S., Rivkin, R. B., Hale, M. S., Kiene, R. P., Price, N. M.,
709 and Li, W. K. W.: DMSP and DMS dynamics during a mesoscale iron fertilization experiment in the Northeast
710 Pacific-Part II: Biological cycling, 53, 2370–2383, https://doi.org/10.1016/j.dsr2.2006.05.022, 2006.

711 Nelson, N. B. and Siegel, D. A.: The Global Distribution and Dynamics of Chromophoric Dissolved Organic
712 Matter, Annu. Rev. Mar. Sci., 5, 447–476, https://doi.org/10/dcwcbk, 2013.

713 Nemcek, N., Ianson, D., and Tortell, P. D.: A high-resolution survey of DMS, CO2, and O2/Ar distributions in
714 productive coastal waters, Global Biogeochem. Cycles, 22, 1–13, https://doi.org/10.1029/2006gb002879, 2008.

715 Nevitt, G. A.: Sensory ecology on the high seas: the odor world of the procellariiform seabirds, Journal of
716 Experimental Biology, 211, 1706–1713, https://doi.org/10/d2rdz3, 2008.

Nightingale, P. D., Malin, G., Law, C. S., Watson, A. J., Liss, P. S., Liddicoat, M. I., Boutin, J., and Upstill-Goddard, R. C.: In situ evaluation of air-sea gas exchange parameterizations using novel conservative and volatile tracers, Global Biogeochem. Cycles, 14, 373–387, https://doi.org/10/d9dztz, 2000.

Okkonen, S. R., Jacobs, G. A., Joseph Metzger, E., Hurlburt, H. E., and Shriver, J. F.: Mesoscale variability in the boundary currents of the Alaska Gyre, Continental Shelf Research, 21, 1219–1236, https://doi.org/10/dc2n79, 2001.

Roshan, S. and DeVries, T.: Efficient dissolved organic carbon production and export in the oligotrophic ocean, Nat Commun, 8, 2036, https://doi.org/10/gcrfdg, 2017.

Royer, S.-J., Levasseur, M., Lizotte, M., Arychuk, M., Scarratt, M. G., Wong, C. S., Lovejoy, C., Robert, M., Johnson, K., Peña, A., Michaud, S., and Kiene, R. P.: Microbial dimethylsulfoniopropionate (DMSP) dynamics along a natural iron gradient in the northeast subarctic Pacific, 55, 1614–1626, https://doi.org/10/ch6cqb, 2010.

Royer, S.-J., Galí Tàpias, M., Saltzman, E., Mccormick, C., Bell, T., and Simó, R.: Development and validation of a shipboard system for measuring high-resolution vertical profiles of aqueous dimethylsulfide concentrations using chemical ionisation mass spectrometry, Environmental Chemistry, https://doi.org/10/f6c3qp, 2014.

Royer, S.-J., Mahajan, A. S., Galí, M., Saltzman, E., and Simó, R.: Small-scale variability patterns of DMS and phytoplankton in surface waters of the tropical and subtropical Atlantic, Indian, and Pacific Oceans, Geophys. Res. Lett., 42, 475–483, https://doi.org/10/gkxzf6, 2015.

Royer, S.-J., Galí, M., Mahajan, A. S., Ross, O. N., Pérez, G. L., Saltzman, E. S., and Simó, R.: A high-resolution time-depth view of dimethylsulphide cycling in the surface sea, Sci. Rep., 6, 32325, https://doi.org/10.1038/srep32325, 2016.

Saltzman, E. S., Bruyn, W. J. D., Lawler, M. J., Marandino, C. A., and McCormick, C. A.: A chemical ionization mass spectrometer for continuous underway shipboard analysis of dimethylsulfide in near-surface seawater, Ocean Sci., 10, https://doi.org/10/bv59ng, 2009.

Schmidtko, S., Johnson, G. C., and Lyman, J. M.: MIMOC: A global monthly isopycnal upper-ocean climatology with mixed layers, J. Geophys. Res. Oceans, 118, 1658–1672, https://doi.org/10/ggqp4h, 2013.

Sheehan, C. E. and Petrou, K.: Dimethylated sulfur production in batch cultures of Southern Ocean phytoplankton, Biogeochemistry, 147, 53–69, https://doi.org/10/ghjqgm, 2020.

Simó, R. and Dachs, J.: Global ocean emission of dimethylsulfide predicted from biogeophysical data, Global Biogeochem. Cycles, 16, 26-1-26–10, https://doi.org/10/cmqkh2, 2002.

Simó, R. and Vila-Costa, M.: Ubiquity of algal dimethylsulfoxide in the surface ocean: Geographic and temporal distribution patterns, Marine Chemistry, 100, 136–146, https://doi.org/10/bg5bph, 2006.

Slezak, D., Brugge, A., and Herndl, G.: Impact of solar radiation on the biological removal of dimethylsulfoniopropionate and dimethylsulfide in marine surface waters, Aquat. Microb. Ecol., 25, 87–97, https://doi.org/10/ftjwjd, 2001.

751 Spiese, C. and Tatarkov, E.: Dimethylsulfoxide reduction activity is linked to nutrient stress in Thalassiosira
752 pseudonana NCMA 1335, Mar. Ecol. Prog. Ser., 507, 31–38, https://doi.org/10.3354/meps10842, 2014.

753 Spiese, C. E., Kieber, D. J., Nomura, C. T., and Kiene, R. P.: Reduction of dimethylsulfoxide to dimethylsulfide
754 by marine phytoplankton, Limnology and Oceanography, 54, 560–570,
755 https://doi.org/10.4319/lo.2009.54.2.0560, 2009.

756 Stefels, J.: Physiological aspects of the production and conversion of DMSP in marine algae and higher plants,
757 Journal of Sea Research, 43, 183–197, https://doi.org/10.1016/S1385-1101(00)00030-7, 2000.

758 Steiner, N. S., Robert, M., Arychuk, M., Levasseur, M. L., Merzouk, A., Peña, M. A., Richardson, W. A., and
759 Tortell, P. D.: Evaluating DMS measurements and model results in the Northeast subarctic Pacific from 1996–
760 2010, Biogeochemistry, 110, 269–285, https://doi.org/10/b99pfb, 2012.

761 Strzepek, R. F. and Harrison, P. J.: Photosynthetic architecture differs in coastal and oceanic diatoms, Nature,
762 431, 689–692, https://doi.org/10/fk2fs7, 2004.

763 Sunda, W. G., Kieber, D., and Kiene, R. P.: An antioxidant function of DMSP and DMS in marine algae Oceanic
764 dimethylsulfide (DMS) photolysis, Nature, 418, 317–320, https://doi.org/10.1038/nature00851, 2002.

765 Taalba, A., Xie, H., Scarratt, M. G., Bélanger, S., and Levasseur, M.: Photooxidation of dimethylsulfide (DMS)
766 in the Canadian Arctic, Biogeosciences, 10, 6793–6806, https://doi.org/10/f5jhsv, 2013.

767 Toole, D. A., Slezak, D., Kiene, R. P., Kieber, D. J., and Siegel, D. A.: Effects of solar radiation on
768 dimethylsulfide cycling in the western Atlantic Ocean, Deep Sea Research Part I: Oceanographic Research
769 Papers, 53, 136–153, https://doi.org/10/brct7m, 2006.

770 Tortell, P. D.: Dissolved gas measurements in oceanic waters made by membrane inlet mass spectrometry,
771 Limnology and Oceanography: Methods, 3, 24–37, https://doi.org/10/drmjv5, 2005a.

772 Tortell, P. D.: Small-scale heterogeneity of dissolved gas concentrations in marine continental shelf waters,
773 Geochemistry, Geophysics, Geosystems, 6, https://doi.org/10/bgqvs9, 2005b.

774 del Valle, D. A., Kieber, D. J., Bisgrove, J., and Kiene, R. P.: Light-Stimulated Production of Dissolved DMSO
775 by a Particle-Associated Process in the Ross Sea, Antarctica, Limnology and Oceanography, 52, 2456–2466,
776 https://doi.org/10.4319/lo.2007.52.6.2456, 2007.

777 Vallina, S. M. and Simó, R.: Strong relationship between DMS and the solar radiation dose over the global
778 surface ocean, Science, 315, 506–508, https://doi.org/10.1126/science.1133680, 2007.

779 Vance, T., Davidson, A., Thomson, P., Levasseur, M., Lizotte, M., Curran, M., and Jones, G.: Rapid DMSP
780 production by an Antarctic phytoplankton community exposed to natural surface irradiances in late spring, Aquat.
781 Microb. Ecol., 71, 117–129, https://doi.org/10/gmw5hv, 2013.

782 Vila-Costa, M., Valle, D. A. D., González, J. M., Slezak, D., Kiene, R. P., Sánchez, O., and Simó, R.:
783 Phylogenetic identification and metabolism of marine dimethylsulfide-consuming bacteria, 8, 2189–2200,
784 https://doi.org/10.1111/j.1462-2920.2006.01102.x, 2006.

785 Wang, W.-L., Song, G., Primeau, F., Saltzman, E. S., Bell, T. G., and Moore, J. K.: Global ocean dimethyl
786 sulfide climatology estimated from observations and an artificial neural network, Biogeosciences, 17, 5335–5354,
787 https://doi.org/10/ghn33p, 2020.

788 Watanabe, Y. W., Yoshinari, H., Sakamoto, A., Nakano, Y., Kasamatsu, N., Midorikawa, T., and Ono, T.:
789 Reconstruction of sea surface dimethylsulfide in the North Pacific during 1970s to 2000s, Marine Chemistry,
790 103, 347–358, https://doi.org/10/bzz33z, 2007.

791 Webb, A. L., van Leeuwe, M. A., den Os, D., Meredith, M. P., J. Venables, H., and Stefels, J.: Extreme spikes in
792 DMS flux double estimates of biogenic sulfur export from the Antarctic coastal zone to the atmosphere, Sci.
793 Rep., 9, 2233, https://doi.org/10/ghjqgc, 2019.

794 Weber, T., Wiseman, N. A., and Kock, A.: Global ocean methane emissions dominated by shallow coastal
795 waters, Nat. Commun., 10, 4584, https://doi.org/10/gf9pc7, 2019.

796 Westberry, T. K., Behrenfeld, M. J., Milligan, A. J., and Doney, S. C.: Retrospective satellite ocean color analysis
797 of purposeful and natural ocean iron fertilization, Deep Sea Research Part I: Oceanographic Research Papers, 73,
798 1–16, https://doi.org/10/f4rcbn, 2013.

799 Westberry, T. K., Shi, Y. R., Yu, H., Behrenfeld, M. J., and Remer, L. A.: Satellite-Detected Ocean Ecosystem
800 Response to Volcanic Eruptions in the Subarctic Northeast Pacific Ocean, Geophys. Res. Lett., 46, 11270–11280,
801 https://doi.org/10/ggr9ms, 2019.

802 Whitney, F. A., Crawford, W. R., and Harrison, P. J.: Physical processes that enhance nutrient transport and
803 primary productivity in the coastal and open ocean of the subarctic NE Pacific, Deep Sea Research Part II:
804 Topical Studies in Oceanography, 52, 681–706, https://doi.org/10/dkn9sn, 2005.

805 Yang, S., Chang, B. X., Warner, M. J., Weber, T. S., Bourbonnais, A. M., Santoro, A. E., Kock, A., Sonnerup, R.
806 E., Bullister, J. L., Wilson, S. T., and Bianchi, D.: Global reconstruction reduces the uncertainty of oceanic
807 nitrous oxide emissions and reveals a vigorous seasonal cycle, Proc Natl Acad Sci USA, 117, 11954–11960,
808 https://doi.org/10/ghc3hw, 2020.

809 Zavarsky, A., Goddijn-Murphy, L., Steinhoff, T., and Marandino, C. A.: Bubble-Mediated Gas Transfer and Gas
810 Transfer Suppression of DMS and CO2, 123, 6624–6647, https://doi.org/10.1029/2017JD028071, 2018.

811 Zeng, C., Rosengard, S. Z., Burt, W., Peña, M. A., Nemcek, N., Zeng, T., Arrigo, K. R., and Tortell, P. D.:
812 Optically-derived estimates of phytoplankton size class and taxonomic group biomass in the Eastern Subarctic
813 Pacific Ocean, Deep Sea Research Part I: Oceanographic Research Papers, 136, 107–118,
814 https://doi.org/10.1016/j.dsr.2018.04.001, 2018.

815